Packed Bed Scrubber for Marine Exhaust Gas Cleaning

Poulsen, Mathias

DOI (link to publication from Publisher):
10.54337/aau504479182

Publication date:
2022

Document Version
Publisher's PDF, also known as Version of record

PACKED BED SCRUBBER FOR MARINE EXHAUST GAS CLEANING

BY
MATHIAS POULSEN

DISSERTATION SUBMITTED 2022

AALBORG UNIVERSITY
DENMARK

Packed Bed Scrubber for Marine Exhaust Gas Cleaning

Ph.D. Dissertation

Mathias Poulsen

Dissertation submitted July, 2022

Dissertation submitted: July, 2022

PhD supervisor: Assoc. Prof. Kim Sørensen
Aalborg University

Assistant PhD supervisor: Assoc. Prof. Thomas Condra
Aalborg University

PhD committee: Associate Professor Samuel Simon Araya
Aalborg University, Denmark

Professor Erik Dahlquist
Malardalen University, Sweden

Professor Brian Elmegaard
Technical University of Denmark, Denmark

PhD Series: Faculty of Engineering and Science, Aalborg University

Department: AAU Energy

ISSN (online): 2446-1636
ISBN (online): 978-87-7573-873-1

Published by:
Aalborg University Press
Kroghstræde 3
DK – 9220 Aalborg Ø
Phone: +45 99407140
aauf@forlag.aau.dk
forlag.aau.dk

Printed in Denmark by Stibo Complete, 2022

Abstract

The use of scrubbers in the maritime industry has seen a significant increase in the past decade due to the implementation of new environmental legislation passed by the International Maritime Organisation. The new legislation stated that by 2020, no vessel would be allowed to emit exhaust gas produced by the combustion of fuel oil containing more than 0.5% sulphur by mass.

To be able to continue the use of fuel oil containing more than 0.5% sulphur by mass, a scrubber can be installed aboard the ship capturing the sulphur contained in the exhaust gas. Marine scrubbers exists in different designs and typically operates in either open- or closed-loop. In open-loop the scrubber uses seawater to remove the SO_2 from the exhaust gas, whereas in closed-loop freshwater is used where alkali substances have to be added to neutralise the acid produced in the scrubber.

Computational Fluid Dynamics (CFD) has become a popular tool for modelling scrubbers, as it provides the basis for capturing interfacial forces, chemistry and heat- and mass transfer. Furthermore, it can provide a possibility to examine phenomena and tendencies that occur inside industrial scale scrubbers, which is a cumbersome, if not impossible, task to achieve on installations on this size.

In this work a model based on the Eulerian-Eulerian CFD framework is developed for a packed bed scrubber. The model incorporates several submodels for both the packed bed and dispersed droplets. Among these are interfacial forces in the packed bed, heat- and mass transfer in the two regimes of the scrubber, and a chemistry model that accounts for the reactions in seawater when SO_2 is absorbed. Additionally custom boundary conditions for the nozzles in scrubbers have been developed, which accounts for droplet size, liquid volume fraction and liquid velocity.

The completed model was used to calibrate the coefficients for the heat and mass transfer in the packed bed, using data gathered from an ocean going vessel. Comparing the calibrated model results to the data, it was found that the model was able to predict the pressure loss to within 3%, exhaust gas and seawater temperatures to within 3% and 3.5%, respectively, and SO_2 content between -24% and 25%. Although the latter seems like a

large error; due to the low concentrations of SO_2 measured at the outlet of the scrubber the absolute difference were not more than 5 ppm for five out of the six data points.

This model can be used to improve new generations of packed bed scrubbers as it allows for optimising aspects such as water consumption, pressure loss, SO_2 removal efficiency, and distribution of seawater in the packed bed, to be addressed.

Resumé

Brugen af scrubbere i den maritime industri har oplevet en betydelig stigning i det seneste årti på grund af implementeringen af ny miljølovgivning vedtaget af den Internationale Søfartsorganisation. Med den nye lovgivning blev det vedtaget, at i 2020 måtte intet fartøj have lov til at udsende udstødningsgas produceret ved forbrænding af skibsolie indeholdende mere end 0,5% svovl på massebasis.

For at kunne fortsætte brugen af skibsolie, der indeholder mere end 0,5 % svovl på massebasis, kan der installeres en scrubber ombord på skibet, som opfanger svovlen i udstødningsgassen. Marine scrubbere findes i forskellige designs og fungerer typisk i enten åben eller lukket kredsløb. I et åbent kredløb bruger scrubberen havvand til at fjerne SO_2 fra udstødningsgassen, mens der et i lukket kredsløb anvendes ferskvand, hvor der skal tilsættes et basiske stof for at neutralisere den syre, der dannes i scrubberen.

Computational Fluid Dynamics (CFD) er blevet et populært værktøj til modellering af scrubbere, da det giver grundlaget for at fange grænsefladekræfter, kemi og varme- og masseoverførsel. Ydermere kan det give mulighed for at undersøge fænomener og tendenser, der opstår inde i scrubbere på industriel skala, hvilket er en besværlig, hvis ikke umulig, opgave at udføre på installationer af denne størrelse.

I dette projekt er der udviklet en model til en packed bed scrubber, baseret på den Eulerske- Eulerske CFD-metode. Modellen inkorporerer flere undermodeller for både packed bed og dråber. Blandt disse er grænsefladekræfter i packed bed, varme- og masseoverførsel i scrubberens to regimer og en kemimodel, der redegør for reaktionerne i havvand, når SO_2 absorberes. Derudover er der udviklet brugerdefinerede randbetingelser for dyserne i scrubbere, som tager højde for dråbestørrelse, væskevolumenfraktion og væskehastighed.

Den færdige model blev brugt til at kalibrere koefficienterne for varme- og masseoverførslen i packed bed ved hjælp af data indsamlet fra et fartøj på havet. Ved at sammenligne de kalibrerede modelresultater med dataene viste det sig, at modellen var i stand til at forudsige tryktabet inden for 3%, udstødningsgas- og havvandstemperaturer inden for henholdsvis 3% og 3,5%

og SO_2 indhold mellem -24% og 25%. Selvom det sidste virker som en stor fejl, så er der på grund af de lave koncentrationer af SO_2 målt ved udløbet af scrubberen ikke mere end 5 ppm i absolutte forskel mellem modellen og dataene for fem ud af de seks datapunkter.

Denne model kan bruges til at forbedre nye generationer af packed bed scrubbere, da den giver mulighed for at optimere aspekter som vandforbrug, tryktab, SO_2 fjernelseseffektivitet og fordeling af havvand i packed bed.

Nomenclature

a	Specific surface area	m^{-1}
a_{Ph}	Phase interface specific surface area	m^{-1}
A	Area	m^2
A_T	Total alkalinity	$\mathrm{mol\,kg}^{-1}$
$\mathcal{A}$	Viscous packing coefficient	
$\mathcal{B}$	Inertial packing coefficient	
b	Molal concentration	$\mathrm{mol\,kg}^{-1}$
C_d	Drag coefficient	
C_K	Packing specific heat transfer constant	
C_h	Packing specific mass transfer constant	
D	Diffusion Coefficient	$\mathrm{m}^2\,\mathrm{s}^{-1}$
D_s	Spreading Coefficient	m
d	Droplet diameter	m
d_{32}	Sauter mean diameter	m
d_h	Hydraulic diameter	m
E	Phase kinetic energy	$\mathrm{m}^2\,\mathrm{s}^{-2}$
F_s	Spread factor	m
$\vec{F}_{ij}$	Interfacial force	$\mathrm{N\,m}^{-3}$
Fr	Froude number	
f	Volume fraction of droplet size	
$\vec{g}$	Gravitational acceleration	$\mathrm{m\,s}^{-2}$
h	Mass transfer coefficient	s^{-1}
he	Enthalpy	$\mathrm{J\,kg}^{-1}$
H^{cc}	Dimensionless Henry solubility	
H^{cp}	Concentration Henry solubility	
I	Ionic strength	
I_k	Turbulent intensity	
j_0	Bessel function of 0^{th} order	
K	Heat transfer coefficient	$\mathrm{W\,m}^{-3}\,\mathrm{K}^{-1}$
K^*	Equilibrium constant	$\mathrm{mol\,kg}^{-1}$
k	Turbulent kinetic energy	$\mathrm{m}^2\,\mathrm{s}^{-2}$
k'	Oxidation Rate	$\mathrm{mol\,L}^{-1}\,\mathrm{min}^{-1}$

l_{dh}	Turbulent length scale	
$\dot{m}$	Specific mass flow	$\mathrm{kg\,s^{-1}\,m^{-3}}$
MW	Molar mass	$\mathrm{g\,mol^{-1}}$
$n_{i,j}$	Number fraction	
Nu	Nusselt number	
p	Pressure	Pa
Pe	Peclet number	
Pe'	Viscosity modified Peclet number	
$\dot{Q}$	Specific heat transfer	$\mathrm{W\,m^{-3}}$
Re	Reynolds number	
R	Universal gas constant	$\mathrm{J\,K^{-1}\,mol^{-1}}$
r	Radius	m
$\vec{r}$	Radial distance	m
Sc	Schmidt number	
Sh	Sherwood number	
t	Time	s
T	Temperature	K
$\vec{u}$	Velocity	$\mathrm{m\,s^{-1}}$
$\dot{V}$	Volumetric flow rate	$\mathrm{m^3\,s^{-1}}$
X	Mole fraction	
x	Representative volume of droplet bin	$\mathrm{m^3}$
Y	Mass fraction	
z	Charge	
We	Weber number	

Greek letters		
α	Volume faction	
α_{th}	Thermal Diffusivity	$\mathrm{m^2\,s^{-1}}$
β	Daughter size probability distribution	
Γ	Breakup frequency	$\mathrm{s^{-1}}$
γ	Activity coefficient	
ϵ	Turbulent dissipation rate	$\mathrm{m^2\,s^{-2}}$
κ	Thermal conductivity	$\mathrm{W\,m^{-1}\,K^{-1}}$
μ	Viscosity	$\mathrm{Pa\,s}$
ρ	Density	$\mathrm{kg\,m^{-3}}$
σ	Surface tension	$\mathrm{N\,m^{-1}}$
τ	Shear tress	$\mathrm{N\,m^{-2}}$
$\bar{\bar{\tau}}$	Turbulent stress tensor	$\mathrm{kg\,m^{-2}\,s^{-2}}$
θ	Angle	
ω	Specific turbulent dissipation rate	$\mathrm{s^{-1}}$
Subscripts		
br	Breaking	
cr	Critical	
d	Drift	
dis	Dispersion	
g	Gas phase	
i	Index	
l	Liquid phase	
p	Phase Index	
q	Phase Index	
s	Solid phase	

Contents

Preface

This PhD-thesis has been written as the conclusion to an industrial PhD carried out as a cooperation between ME Production A/S and Aalborg University. This project was supervised by Kim Sørensen from Aalborg University and Henrik Vejergang from ME Production A/S. Funding for the project was provided by Innovation Fund Denmark [8053-00053B] and ME Production A/S.

This thesis is presented as a collection of papers and the following is summary linking these papers together into this project. The four papers created during this study are:

Paper A: Mathias Poulsen, Kim Sørensen, Thomas Condra. Heat and Mass Transfer Model for Droplets with Internal Circulation, Linköping Electronic Conference Proceedings Vol.176(25), pp. 175–202, 2021.

Paper B: Mathias Poulsen, Kim Sørensen, Thomas Condra. Comparison of Two-Phase Porosity Models for High Capacity Random Packing, E3S Web Conf. Vol. 321, 01015, 2021.

Paper C: Mathias Poulsen, Kim Sørensen, Thomas Condra. Optimisation of exhaust covers in marine scrubbers, accepted in Journal of Fluids Engineering, 2022

Paper D: Mathias Poulsen, Henrik Ström, Srdjan Sasic, Kim Sørensen, Thomas Condra. Development and calibration of a model for packed bed marine scrubbers aboard ocean-going vessels, under review, 2022.

I would like to extend my gratitude to Henrik Ström and Srdjan Sasic from Chalmers University. They have both have been supportive and extremely helpful in our discussions. Having not met in person due to pandemic, I have still thoroughly enjoyed our cooperation despite it being virtual. Furthermore I would like to thank my supervisors Kim Sørensen and Thomas Condra

who have both been more than helpful in both good and bad times during the project. To my the fantastic colleagues at ME Production, thank you all for helping me in my endeavours and putting up with a lot of my questions. Lastly I would like to thank my girlfriend Tina for supporting me and making it possible for me to spend the time required to undertake this work; specially in the time when writing this thesis, where you have not only taken care of me, but also our newly arrived son Asger.

Part I

Project

Chapter 1

Introduction

The process of removing sulphur oxides (SO_x) from exhaust gases has been of interest to industry since the beginning of the 20th century. Initially the capture of sulphur from the exhaust gas of coal burning processes was intended as a method of producing sulphuric acid for commercial purposes. It was first around 1930 that concerns were raised about the environmental issues caused by the emission of SO_x and the first scrubbers were installed on power stations around England [1].

The scene for the use of scrubbers in the maritime industry was set in 1997, when the International Maritime Organisation (IMO) adopted the Annex VI of the MARPOL convention. Here it was stated that the sulphur content of the fuel oils used globally must not exceed 4.5% by mass and that it must not exceed 1.5% by mass in the Baltic Sea by 2005. To meet the more stringent legislation in the Baltic Sea the shipowners were presented with two options; either switch to a compliant fuel or use any other technological method to limit their emission of SO_x [2].

Since the ratification of Annex VI other areas have adopted the same regulations as in the Baltic Sea and these are now termed the Emission Control Areas(ECA). In figure 1.1 the ECA as it looks in 2021 is shown [3]:

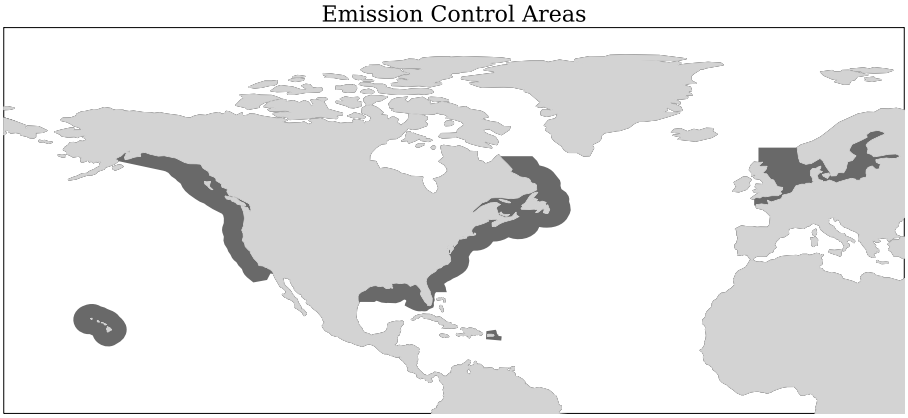

Fig. 1.1: Emission Control Areas as defined by the IMO shown in dark grey. [3, 4]

Over the years, since the adoption of Annex IV, the allowable sulphur content has gradually been decreased both globally and in the ECA. The timeline for the implementation of these reductions is shown in figure 1.2 [5]:

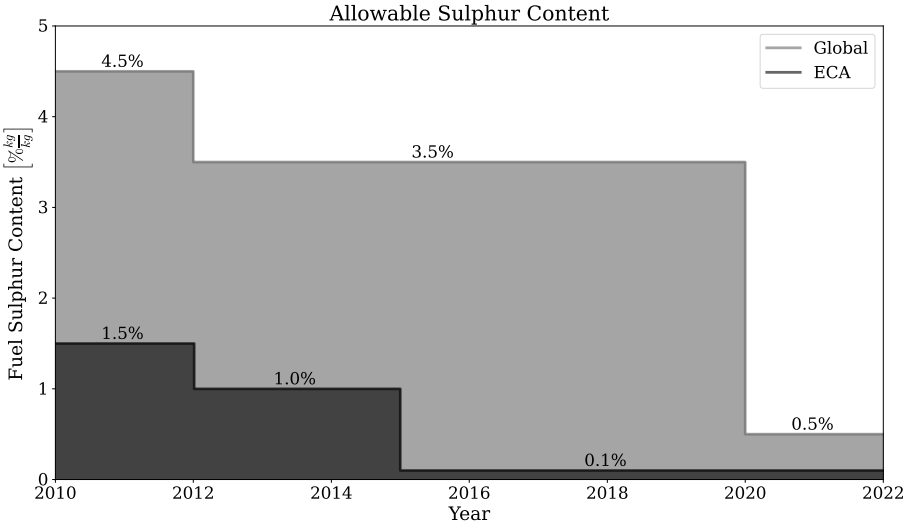

Fig. 1.2: Timeline for the permissible fuel sulphur content globally and in ECA [5]

It was first in 2016, when the IMO announced that the global sulphur cap would be revised, from 3.5% to 0.5% by mass, by the 1 of January 2020, that interest from shipowners was shown in scrubbers.

In 2016 the IMO announced that the global sulphur cap would be revised from from 3.5% to 0.5% by mass. This peaked the interest in scrubbers as

shipowners were forced to take action. Prior to this it was easier and cheaper to just switch to a compliant fuel if a ship was to enter the ECA, as the sulphur content of the Heavy Fuel Oil (HFO) was already compliant. However, with the new legislation, exclusively using compliant fuel would increase fuel cost significantly which made the business case for installing a scrubber as a method for reaching compliance attractive .

Using the concentration of SO_x in exhaust gas directly as a measure of compliance is not ideal as it would be possible to simply dilute the exhaust gas with ambient air to reduce the concentration of SO_x. As the sulphur in the exhaust gas originates from fuel oil, a comparative measure related to the CO_2 produced by the combustion is made. Based on the global average the IMO has correlated the following emission ratios to the sulphur content in the fuel oil [6]:

Sulphur content $\%\ \frac{kg}{kg}$	Emission ratio $\frac{SO_2}{CO_2}\ \frac{ppm}{\%v/v}$
4.5	195.0
3.5	151.7
1.5	65.0
1.0	43.3
0.5	21.7
0.1	4.3

Table 1.1: SO_2 / CO_2 ratio for equivalent fuel sulphur content [6]

1 Scrubber Types

Generally there are two types of scrubber designs used in the maritime industry, which are inline and U-type scrubbers. The difference between these two types of scrubber designs is the path that the exhaust gas has to take to pass through the scrubber. In figure 1.3a a schematic of an inline scrubber is shown, here it can be seen that the exhaust gas inlet and outlet are placed inline with each other on the centreline of the scrubber thereby giving it its name. For the u-type scrubber, where a schematic is shown in figure 1.3b, the exhaust gas inlet and outlet both faces upwards. This forces the gas to make a u-turn in the scrubber, hence its name u-type.

Each scrubber design comes with its pros and cons in terms of space requirements, manufacturability, and design. An important criteria when injecting a liquid into the exhaust gas system is to ensure its containment and prevent backflow. This is handled for the inline scrubber by installing an exhaust cover over the exhaust inlet as shown in figure 1.3a. The exhaust cover ensures that the liquid injected from above does not flow back into the exhaust gas system. For the u-type scrubber the design of the scrubber body itself handles the issue with potential back flow as the exhaust inlet faces downwards and is elevated well above the bottom of scrubber. Although the scrubbers shown in figure 1.3 are not to scale, it is clear that for a scrubber with the same cross sectional area in the main body, the u-type scrubber has a larger footprint compared to the inline scrubber. Because floor space is a premium aboard ships inline scrubbers are often used for retrofits on existing vessels where the layout of the deck plan was not made with a scrubber in mind.

The prime objective for a scrubber is to create a larger interfacial area between the liquid and exhaust gas to facilitate the absorption of SO_2. There are generally two methods by which the interfacial area between the liquid and exhaust gas can be created. One is to use a packed bed as shown in 1.3a. Here, a packing material is used to slow down the liquid and create a large interfacial area between the liquid and exhaust gas as the liquid flows along the surfaces of the packing material. The other method for creating the interfacial area between the exhaust gas and liquid, is to use sprays to create a dispersed mist of droplets which is shown in 1.3b. These two methods are not fixed to the specific type of scrubber design, meaning the an inline scrubber can be designed for operation as a spray scrubber and a u-type scrubber can be designed to operate as a packed bed scrubber.

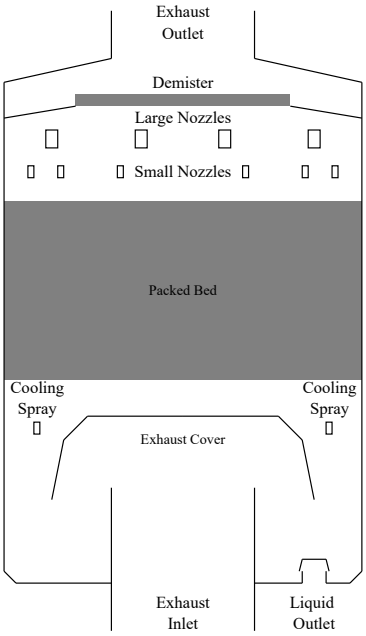

(a) Inline scrubber, using a packed bed to achieve the interfacial area between the scrubbing liquid and exhaust gas.

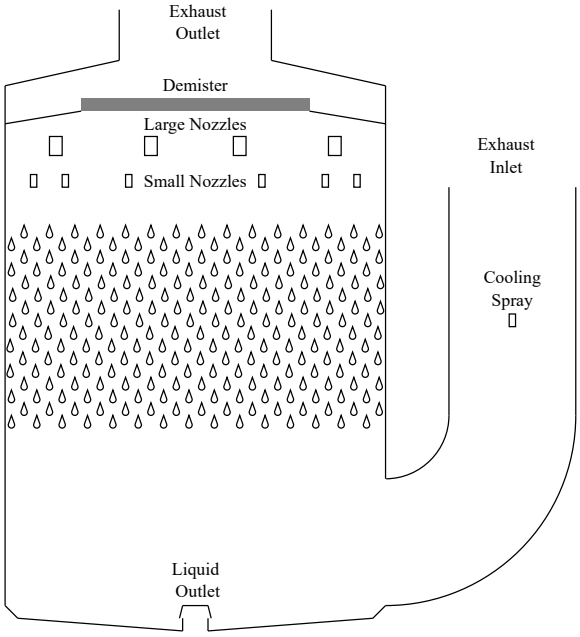

(b) U-type scrubber, using sprays to achieve the interfacial area between the scrubbing liquid and exhaust gas.

Fig. 1.3: Scrubber designs generally used in the maritime industry and the methods used to create a large interfacial area between the liquid and exhaust gas.

2 Scrubber Systems

Besides the scrubber design and the method for creating the interfacial area, there is also the system for handling of liquid used in the scrubbing process. For marine scrubbers seawater is an ideal liquid as it readily available and acts as buffer due to is natural alkalinity [7]. A scrubber system using seawater as the scrubbing liquid is called an open loop system and can be seen in figure 1.4. In an open-loop system the seawater is pumped from below the waterline and up to the scrubber, which is placed near the smoke stack at the top of ship. Once the seawater has passed through the scrubber it is discharged back into the ocean, through an outlet in the hull below the waterline.

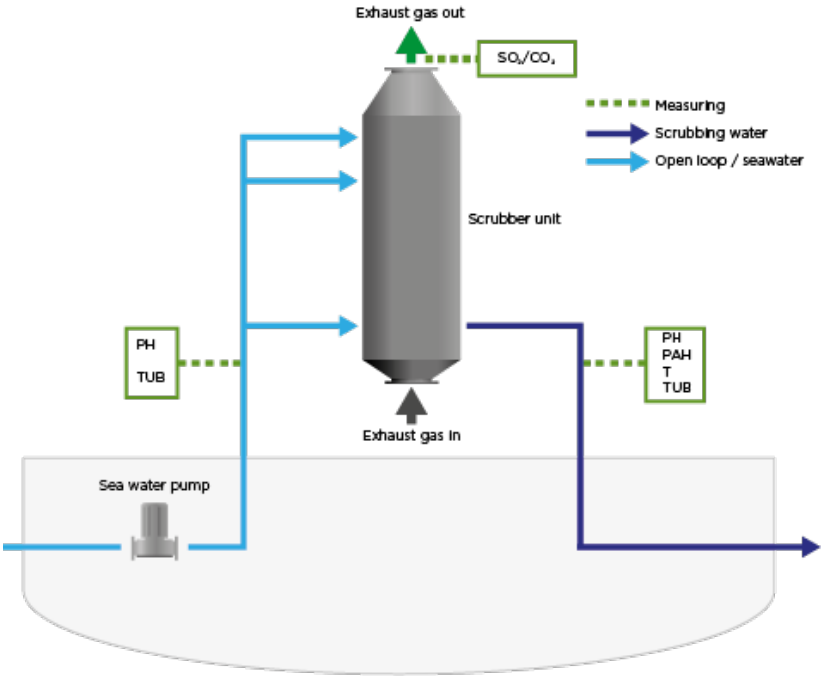

Fig. 1.4: Open-loop scrubber system [8].

A different approach is to use a closed-loop scrubbing system, which is shown in figure 1.5. Here, the water from scrubbing process is recycled after it has been through the scrubber. It does however require more auxiliary equipment to use a closed loop system as the build up of sulphur species causes the pH of the water to increase and at the same time residual fuel and other impurities accumulate in the process water. To neutralise the acid produced by the absorption of SO_2 an alkali substance is added to process

water as it is recirculated. Additionally the sludge formed by the residual fuel and impurities have to be separated from the process water and stored aboard until the vessel can discharge it when at port. Lastly a heat exchanger is necessary to cool the system as heat from the exhaust gas is transferred to the process water. With the auxiliary equipment and the need for continuously adding an alkali substance to the process water this type of scrubber system is comparatively more expensive in both initial investment and operation cost, compared to an open-loop scrubber system.

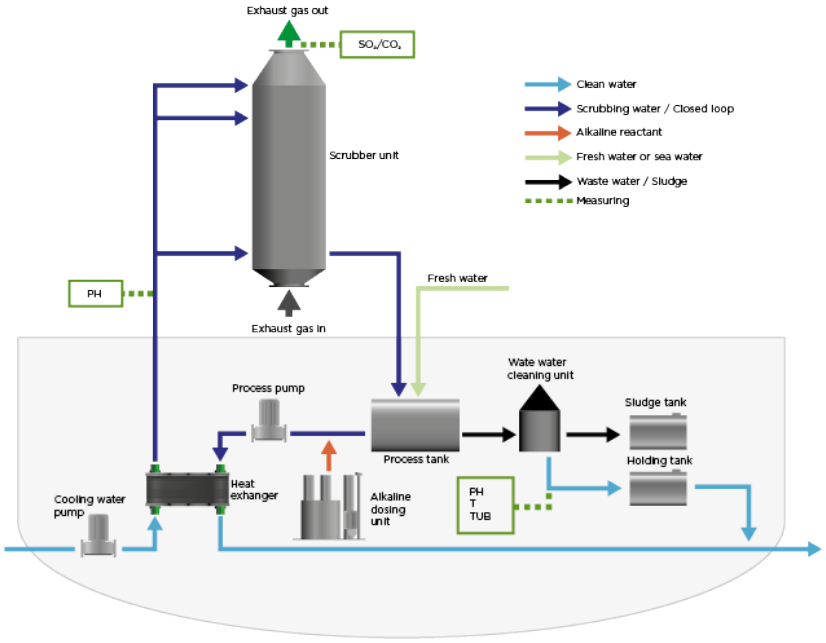

Fig. 1.5: Closed-loop scrubber system [8]

A hybrid of the two systems also exists and is opted for if the route of the vessel often crosses into areas where the discharge of seawater from an open-loop scrubber system is banned. For example discharge is banned in both the Suez and Panama canal and in the domestic emission control areas of China [9]. As a hybrid system has the ability to switch between open- and closed-loop operation, it is often selected over a closed-loop system as its initial investment cost is only slightly higher, but provides the operator with the option of only running in the more expensive closed-loop mode when sailing in a discharge ban area.

3 State Of The Art

Spray scrubbers have been thoroughly studied in the literature, where computational fluid dynamics (CFD) has been used as a tool. Simulations of spray u-type scrubbers for SO_2 absorption with a limestone slurry on power plants have been investigated using both an Eulerian-Eulerian and an Eulerian-Lagrange framework [10–12]. In all these studies interfacial forces, chemistry and heat- and mass transfer was accounted for and the models results were in good agreement with the experimental results.

The absorption of SO_2 in seawater has been presented in studies relating to both pure chemistry and in relation to absorption in a single droplet of seawater [7, 13, 14]. In these studies various species and their reactions are accounted for. However, the two studies relating to pure chemistry account for a different number species and have different approaches in their methods, though they both show good agreement with experimental data [7, 13]

An Eulerian-Lagrange model of an inline spray scrubber using seawater has been presented. Here chemisty, droplet heat- and mass transfer, and wall films were considered. The model was correlated to data and showed error of around 10% on pressure loss, SO_2 absorption and temperature [15].

Packed bed scrubbers have been modelled as chemical reactors and typically only in one dimension parallel to the flow direction of the flue gas. In these models flow patterns and pressure loss are neglected, and only the removal of sulphur is accounted for [16, 17]. More detailed modelling of packed beds consisting of small packing elements have been presented [18, 19]. In one of the studies, an Eulerian-Eulerian model was used for predicting SO_2 and NO_x in a cylindrical bed with uniform liquid distribution under high pressure. Here the authors found that the removal efficiency of SO_2 was not affected by the high pressure in the packed bed whereas NO_x and CO_2 were [19]. The other study presented the same Eulerian-Eulerian model but only focused on the absorption SO_2, which was modelled for three different 3 packing types [18].

It is clear that spray scrubbers are well described and a lot of modelling approaches are available for this type of scrubber. On the other hand some sub models available for packed bed scrubbers, but the entirety of packed bed scrubbers are not readily available.

4 Objectives

In this project the overall objective was to develop a model of a packed bed inline scrubber operating in open-loop mode. The model should be relatively rapid to evaluate so as to be suitable for optimising future scrubber designs

and design changes to current scrubber models in an industrial setting. To fulfil the objectives set, the following had to be achieved:

- A detailed understanding of the heat- and mass transfer processes inside and outside the packed bed
- Knowledge of the influence of liquid distribution on the removal efficiency of the packed bed
- A sufficient understanding of the chemical reaction processes that occur with the seawater and to incorporate this into the scrubber model.
- As this project has ties to industry, a final objective was that the knowledge and experience gained in this project is applicable to a practical design in a commercial setting.

Chapter 2

Modelling

The model for the scrubber is developed in OpenFOAM, which is an open-source C++ library made for solving partial differential equations using the finite volume method [20]. Due to its open source code and availability OpenFOAM has seen a great increase in use by the CFD community in both academia and industry in recent years. Unlike commercial CFD-codes OpenFOAM is not a one in all solver, instead it consists of a series of purpose build solvers which are coded for a specific set of governing equations.

In this work the model is based on the solver called multiphaseEulerFoam which is an Eulerian-Eulerian solver capable of solving for a system of any number of compressible phases with a common pressure [20]. In this frame work each phase has its own momentum, energy and species equation, and the interactions between the phases are handled as source terms in the respective equation set.

The governing equations upon which multiphaseEulerFoam solver is based are presented in the following. The conservation of mass for a phase p is given as:

$$\frac{\partial}{\partial t}\left(\alpha_p \rho_p\right) + \nabla \cdot \left(\alpha_p \rho_p \vec{u}_p\right) = \sum_{q=1}^{n} \left(\dot{m}_{qp} - \dot{m}_{pq}\right) \tag{2.1}$$

where α_p is the volume fraction of phase p, ρ_p is the density, $\vec{u}_p$ is the velocity vector, and $\dot{m}_{qp}$ and $\dot{m}_{pq}$ is the mass between phases p and q.

The momentum equation for phase p can be given as:

$$\begin{aligned} &\frac{\partial}{\partial t}\left(\alpha_p \rho_p \vec{u}_p\right) + \nabla \cdot \left(\alpha_p \rho_p \vec{u}_p \vec{u}_p\right) = \\ &-\alpha_p \nabla p + \alpha_p \rho_p \vec{g} + \nabla \cdot \bar{\bar{\tau}}_p + \sum_{q=1}^{n} \left(\vec{F}_{qp} + \dot{m}_{qp} \vec{u}_{qp} - \dot{m}_{pq} \vec{u}_{pq}\right) \end{aligned} \tag{2.2}$$

where p is the common pressure, $\vec{g}$ is the gravitational acceleration, $\bar{\bar{\tau}}$ is the stress tensor which account for both viscous and turbulent stresses, $\vec{F}_{qp}$ is the interfacial forces between phase q and p, and $\dot{m}_{qp}\vec{u}_{qp}$ and $\dot{m}_{pq}\vec{u}_{pq}$ is the momentum transfer due to mass transfer between the phases q and p.

The energy equation for phase p can be given as:

$$\frac{\partial}{\partial t}\left(\alpha_p \rho_p h e_p\right) + \nabla \cdot \left(\alpha_p \rho_p \vec{u}_p h e_p\right) + \frac{\partial}{\partial t}\left(\alpha_p \rho_p E_p\right) + \nabla \cdot \left(\alpha_p \rho_p \vec{u}_p E_p\right) = \alpha_p \rho_p \vec{u}_p \cdot \vec{g} + \nabla^2 \left(\alpha_p \alpha_{th,p} h e_p\right) + \dot{Q}_{pq} \tag{2.3}$$

where he_p is the enthalpy, E_p is the kinetic energy, α_{th} is the thermal diffusivity, and $\dot{Q}_{pq}$ is the heat transfer between phases q and p.

As both the exhaust gas and seawater consists of multiple species, a species equation is solved for each individual species in each phase. The species equation for phase p can be given as:

$$\frac{\partial}{\partial t}\left(\alpha_p \rho_p Y_{p,k}\right) + \nabla \cdot \left(\alpha_p \rho_p \vec{u}_p Y_{p,k}\right) = \nabla^2 \left(\alpha_p \rho_p D_{p,k} Y_{p,k}\right) + \dot{m}_{pq,k} \tag{2.4}$$

where $Y_{p,k}$ is the mass fraction of species k in phase p, $D_{p,k}$ is the diffusion coefficient, and $\dot{m}_{pq,k}$ is the mass flow of species k from phase q to phase p.

In addition to the solver, a custom thermodynamic and physical library is created to model the phase properties. The expressions used for the seawater and exhaust gas in this library are presented in appendix I

To be able to use the multiphaseEulerFoam solver to model a packed bed scrubber, new correlations for interfacial forces and heat- and mass transfer will have to be added. Furthermore, handling the respective models for in- and outside the packed bed also have to be developed. Lastly the incorporation of chemical reactions into solver also have to be carried out.

Chapter 3

Chemistry

In the following chapter a detailed overview of the chemistry model that is implemented into the model presented in paper D is given. The chemical reactions that occur during the scrubbing process are generally extremely fast and can therefore be treated as equilibria, which results in system of non-linear equations that have to be solved in each iteration of the solution. The absorption of SO_2 in seawater and the equilibria governing the reactions have been presented in various studies throughout the literature [7, 13, 21]. In the equilibria models the number of equilibria considered varies, where some only considers the sulphite species, while others also includes sulphate and carbonate species. In the chemistry model used for this work the following equilibria are considered:

$$SO_{2(aq)} \rightleftharpoons HSO_3^- + H^+ \tag{3.1}$$
$$HSO_3^- \rightleftharpoons SO_3^{2-} + H^+ \tag{3.2}$$
$$HSO_4^- \rightleftharpoons SO_4^{2-} + H^+ \tag{3.3}$$
$$CO_{2(aq)} \rightleftharpoons HCO_3^- + H^+ \tag{3.4}$$
$$HCO_3^- \rightleftharpoons CO_3^{2-} + H^+ \tag{3.5}$$

In addition to the equilibria the oxidation of sulphites, which produces sulphates, is also considered in the chemistry model.

1 Seawater Properties

Compared to pure water, using seawater as the scrubbing liquid requires extra attention to be paid to the chemistry that occurs during the scrubbing process. There are two properties of seawater which have an influence on

the chemical reactions that occur. One property is that seawater is an ionic solution and the other is the natural alkalinity. Both properties depend on the species that make up the saline concentration. The majority of the species that makes up the salinity in standard seawater are presented in Table 3.1 [22]:

Species	$Y_i \times 10^{-3}$	b_i	z_i	MW_i
Cl^-	19.35	0.5658	-1	35.45
Na^+	10.78	0.4861	1	22.99
SO_4^{2-}	2.71	0.0293	-2	96.06
Mg^{2+}	1.28	0.0548	2	24.31
Ca^{2+}	0.41	0.0107	2	40.08
K^+	0.399	0.0106	1	39.10
HCO_3^-	0.108	0.00183	-1	61.02
Br^-	0.067	0.00087	-1	79.90
Sr^{2+}	0.08	0.00009	2	87.62
$B(OH)_3$	0.0198	0.00033	0	51.83
CO_3^{2-}	0.016	0.00027	-2	60.01
$B(OH)_4^-$	0.0079	0.00010	-1	78.84
F^-	0.0013	0.00007	-1	19.00
sum	35.1717	1.16075		

Table 3.1: Standard mean composition of seawater with a salinity of 35 $\frac{g}{kg}$ [22]. In the columns the mass fraction, molality, charge, and molar mass for each species is presented.

A key factor of using seawater as the scrubbing liquid is its natural alkalinity. Alkalinity is a measure of a liquids ability to resist acidification which is caused by weak acids and their conjugate bases acting as a buffer for the solution [23]. The alkalinity of seawater can be given as follows [24]:

$$\begin{aligned} A_T = &\left[HCO_3^-\right] + 2\left[CO_3^{2-}\right] + \left[B(OH)_4^-\right] + \left[OH^-\right] + \left[HPO_4^{2-}\right] \\ &+ 2\left[PO_4^{3-}\right] + \left[SiO\,(OH)_3^-\right] + [NH_3] + \left[HS^-\right] + ... \\ &- \left[H^+\right]_F - \left[HSO_4^-\right] - [HF] - [H_3PO_4] - ... \end{aligned} \tag{3.6}$$

It can bee seen in Equation 3.6 that several species affect the alkalinity of seawater. However, the concentration of many of the species are small compared

to the main contributors, some of which was presented in Table 3.1. In the model for seawater, in this work, the alkalinity is approximated as shown in equation 3.7 [25]:

$$A_T \approx \left[HCO_3^-\right] + 2\left[CO_3^{2-}\right] \tag{3.7}$$

1.1 Activity Coefficient

When modelling ionic solutions the equilibria starts to deviate from the ideal behaviour where the activity of a given species is equal to its concentration. To account for this deviation an activity coefficient for each ionic species is introduced into the equilibrium expressions [26]. By rewriting the expression for an equilibrium equation it can be seen that the introduction only affects the equilibrium constant:

$$K = \frac{\gamma_B[B^-]\gamma_C[C^+]}{[A]} \tag{3.8}$$

$$K^* = K\frac{1}{\gamma_B\gamma_C} = \frac{[B^-][C^+]}{[A]} \tag{3.9}$$

To calculate the activity coefficient for the individual species the Davies equation, given in equation 3.10, is used [27]. This is an empirical extension on the Debye-Hückel equation for weak electrolytic solutions.

$$\ln(\gamma_i) = -Az_i^2\left(\frac{\sqrt{I}}{1+\sqrt{I}} - 0.2I\right) \tag{3.10}$$

$$A = \frac{1.82\times10^6}{(\epsilon T)^{1.5}}$$

$$\epsilon = (87.91 - 0.4044T_C + 9.587\times10^{-4}T_C^2 - 1.328\times10^{-6}T_C^3) \tag{3.11}$$

In Equation 3.10 it can be seen that the activity coefficient depends on the charge of the species, the ionic strength of the solution and the empirical parameter A which depends on temperature and the dielectric constant of the solvent. Here the solvent is pure water and the dielectric constant is correlated with the temperature in °C [28].

The ionic strength for a solution can be calculated as shown in the following equation:

$$I = \frac{1}{2}\sum_{i=1}^{n_{species}} b_i z_i^2 \tag{3.12}$$

However, as not all of the species listed in Table 3.1 are included in the model the ionic strength of the seawater is based in the following empirical correlation [29]:

$$I = \frac{1994 Y_{sal}}{1000 - 1005 Y_{sal}} \tag{3.13}$$

where Y_{sol} is the mass fraction of saline species.

The Davies equation used for determining the activity is only valid for solutions with an ionic strength less than 0.5, corresponding to a salinity of $24.5 \frac{\text{g}}{\text{kg}}$. But, it can be seen in figure 3.1, the activity for seawater with a salinity does not differ significantly.

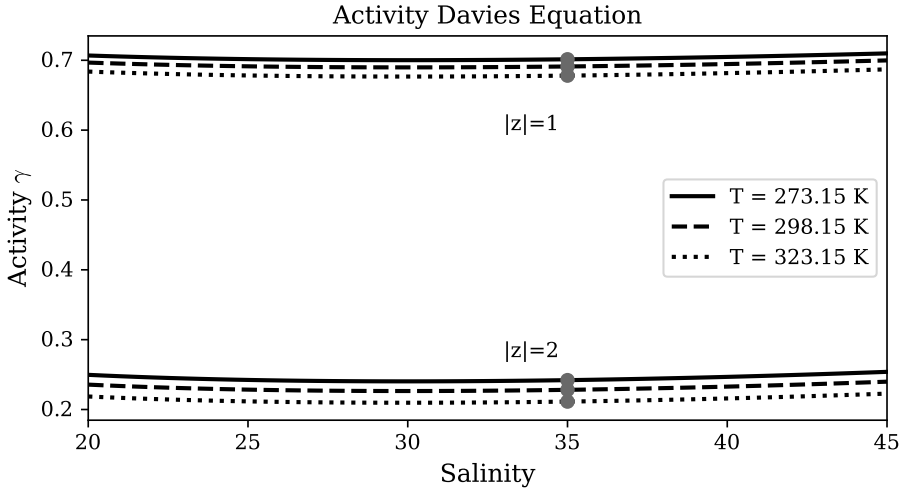

Fig. 3.1: Activity coefficients predicted by the Davies equation for species with charges ± 1 and ± 2 respectively. The grey dots represents the standard seawater with salinity of $35 \frac{\text{g}}{\text{kg}}$.

2 Solution Method

The equilibria presented in equations 3.1, 3.2, 3.3, 3.4 and 3.5 are expressed algebraically through their respective equilibrium constants as follows:

$$K^*_{HSO_3} = \frac{\left[HSO_3^-\right]\left[H^+\right]}{\left[SO_2\right]} \tag{3.14}$$

$$K^*_{SO_3} = \frac{\left[SO_3^{2-}\right]\left[H^+\right]}{\left[HSO_3^-\right]} \tag{3.15}$$

$$K^*_{SO_4} = \frac{\left[SO_4^{2-}\right]\left[H^+\right]}{\left[HSO_4^-\right]} \tag{3.16}$$

$$K^*_{HCO_3} = \frac{\left[HCO_3^-\right]\left[H^+\right]}{\left[CO_2\right]} \tag{3.17}$$

$$K^*_{CO_3} = \frac{\left[CO_3^{2-}\right]\left[H^+\right]}{\left[HCO_3^-\right]} \tag{3.18}$$

The equilibrium constants for equations 3.16, 3.17 and 3.18 have all been determined in seawater [30, 31]. This means that the non-ideal behaviour due to the ionic species in the seawater is accounted for in the expressions for the equilibrium constants. Thus the introduction of activity coefficients presented in equation 3.9 is only applied to the equilibrium constants in equations 3.14 and 3.15. As the expressions for the equilibrium constants are exhaustive correlations, they are presented in appendix II.

For all of the equilibria their equilibrium constants have been calibrated with the concentration of the species expressed in molality. Molality is generally given as the concentration of a substance in moles per kg of solvent. However in some cases it is expressed as moles per kg of mixed solvent, which is the case for the equilibria used in this model. As the framework in OpenFOAM uses mass fraction as a basis for concentration, all concentrations are converted to molality before the equilibria is satisfied and vice versa when the change in species concentration are imposed on the transport equation. The conversion from mass fraction to molality is given as:

$$b_i = \frac{Y_i}{MW_i\, 0.001 \frac{\text{kg}}{\text{g}}} \tag{3.19}$$

The equilibria are solved by introducing a variable which represents the production or consumption of H^+ into each equilibrium equation [32]. Thereby the concentration of each species after the equilibriums are fulfilled can be expressed as:

$$\begin{aligned}
\left[SO_{2(aq)}\right]_a &= [SO_2]_i - b_1 & [CO_2]_a &= [CO_2]_i - b_3 \\
\left[HSO_3^-\right]_a &= \left[HSO_3^-\right]_i + b_1 - b_2 & \left[HCO_3^-\right]_a &= \left[HCO_3^-\right]_i + b_3 - b_4 \\
\left[H^+\right]_a &= \left[H^+\right]_i + b_1 + b_2 + b_3 + b_4 + b_5 & \left[CO_3^-\right]_a &= \left[CO_3^-\right]_i + b_4 \\
\left[SO_3^{2-}\right]_a &= \left[SO_3^{2-}\right]_i + b_2 & \left[HSO_4^-\right]_a &= \left[HSO_4^-\right]_i - b_5 \\
& & \left[SO_4^{2-}\right]_a &= \left[SO_4^{2-}\right]_i + b_5
\end{aligned} \tag{3.20}$$

Combining these expressions with equations 3.14, 3.15, 3.16, 3.17 and 3.18 results in a set of non-linear equation that are solved at each time step. The resulting set of equations are solved using the Newton-Raphson method where the variables from equation 3.20 and equations 3.14-3.18 are put into respective vectors $\mathbf{b} = [b_1, b_2, b_3, b_4, b_5]$ and $\mathbf{f} = [f_1, f_2, f_3, f_4, f_5]$ which results in the following matrix equation for an iteration:

$$\mathbf{b}^{i+1} = \mathbf{b}^i + [\mathbf{B}]^{-1}[-\mathbf{f}] \tag{3.21}$$

where $[\mathbf{B}]$ is the Jacobian matrix of the equilibria which can be given as:

$$[\mathbf{B}] = \begin{bmatrix} \frac{\partial f_1}{\partial b_1} & \cdots & \frac{\partial f_1}{\partial b_5} \\ \vdots & \ddots & \vdots \\ \frac{\partial f_5}{\partial b_1} & \cdots & \frac{\partial f_5}{\partial b_5} \end{bmatrix} \tag{3.22}$$

With equation 3.21 being iterative, a convergence criteria for $\mathbf{b}$ has to be set. Since the concentration of H^+ is on the order of 10^{-9} which is the smallest among the species in the equilibria, the iterations stops when the following condition is met:

$$10^{-12} \leq \max\left(\left|\mathbf{b}^i - \mathbf{b}^{i+1}\right|\right) \tag{3.23}$$

This method requires the system of equations to be solved for each cell in the mesh. To limit the number of iterations required for the system of equations to converge supplying an initial guess for $\mathbf{b}$. Considering that the change in species concentration is limited by the transfer of species between the phases, the change in concentration within a single time step will be small. Therefore the initial guess for $\mathbf{b}$ is simply zero for all variables in the vector.

3 Equilibria Validation

Data for the absorption of SO_2 in seawater and resulting changes in pH has been published in earlier works [13]. The amount of absorbed SO_2 absorbed

is given not only by the SO_2 dissolved in the seawater but also include the sulphite species, which means that the total SO_2 absorbed is given as:

$$[SO_2]_{abs} = [SO_2] + [HSO_3] + [SO_3] \tag{3.24}$$

The initial concentration of the species used for the validation is presented in table 3.2, where the species that are not listed are not present initially.

Species	SO_4^{2-}	HCO_3^-	CO_3^-	H^+
Molality $\frac{\text{mol}}{\text{kg}}$	2.93×10^{-2}	1.83×10^{-3}	2.85×10^{-4}	7.943×10^{-9}

Table 3.2: Initial concentration of species in seawater.

The concentration of SO_4^{2-}, HCO_3^- are taken from table 3.1, whereas the concentration of CO_3^- is calculated using equation 3.7, where the total alkalinity of standard seawater which is 2.4 $\text{mmol}\,\text{kg}^{-1}$ is used [22]. Lastly the concentration of H^+ is calculated from the standard pH of seawater which is 8.1 [22].

In figure 3.2 the comparison between that data and the equilibria model is presented:

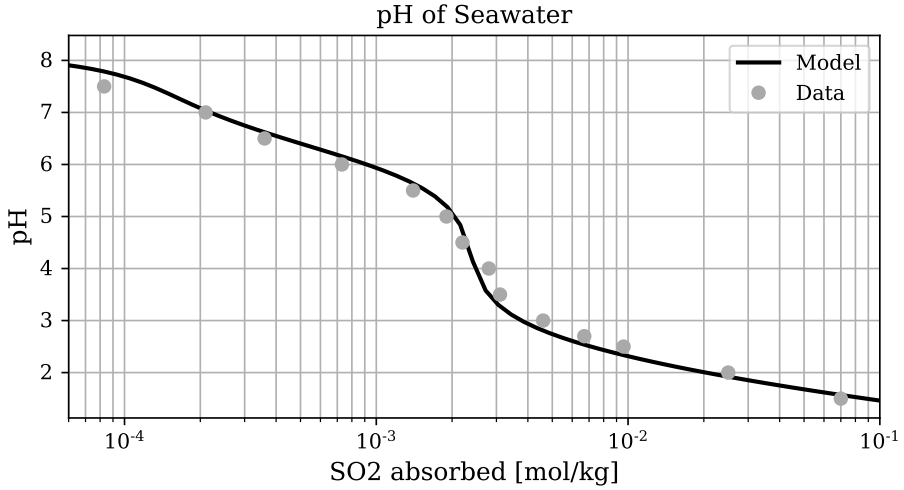

Fig. 3.2: Comparison of equilibria model with data from literature [13].

It can be seen that the model follows the trend in the data well. However, there are discrepancies between the data and the model. The errors are seen around the equivalence point, where the pH is 4, which is where the weak bases present in seawater have been neutralised. Generally the errors are

within $\pm$ 5% with the exception of the three data point with a pH of 4.0, 3.5 and 3.0 where the error is 12, 6 and 6 % respectively. Despite these errors, the general performance of the equilibria model is sufficiently accurate for the scrubber model.

In figure 3.3 concentration of all sulphur and carbon species are shown as the seawater acidifies during the absorption of SO_2. For the sulphite species it can be seen that initially the bulk of the absorbed SO_2 is converted to SO_3^{2-}, but at a pH below 6.5 the equilibria between SO_3^{2-} and HSO_3^-, shown in equation 3.15, goes in favour of HSO_3^- and the concentration of SO_3^{2-} is reduced. From this point on HSO_3^- constitutes the bulk of the sulphite species arising from the the absorption of SO_2.

Additionally it can be seen that at the equivalence point the increase in concentration of HSO_3^- is relatively small. Looking at the carbon species it can also be seen that this corresponds to when the equilibria between HCO_3^- and CO_2 begins to favour CO_2, meaning that all of the bases from the dissolved carbonates have been depleted.

After the equivalence point it can be seen that the concentration of SO_2 begins to increase and at a pH of 2.5 the concentration is rapidly approaching that of HSO_3^-.

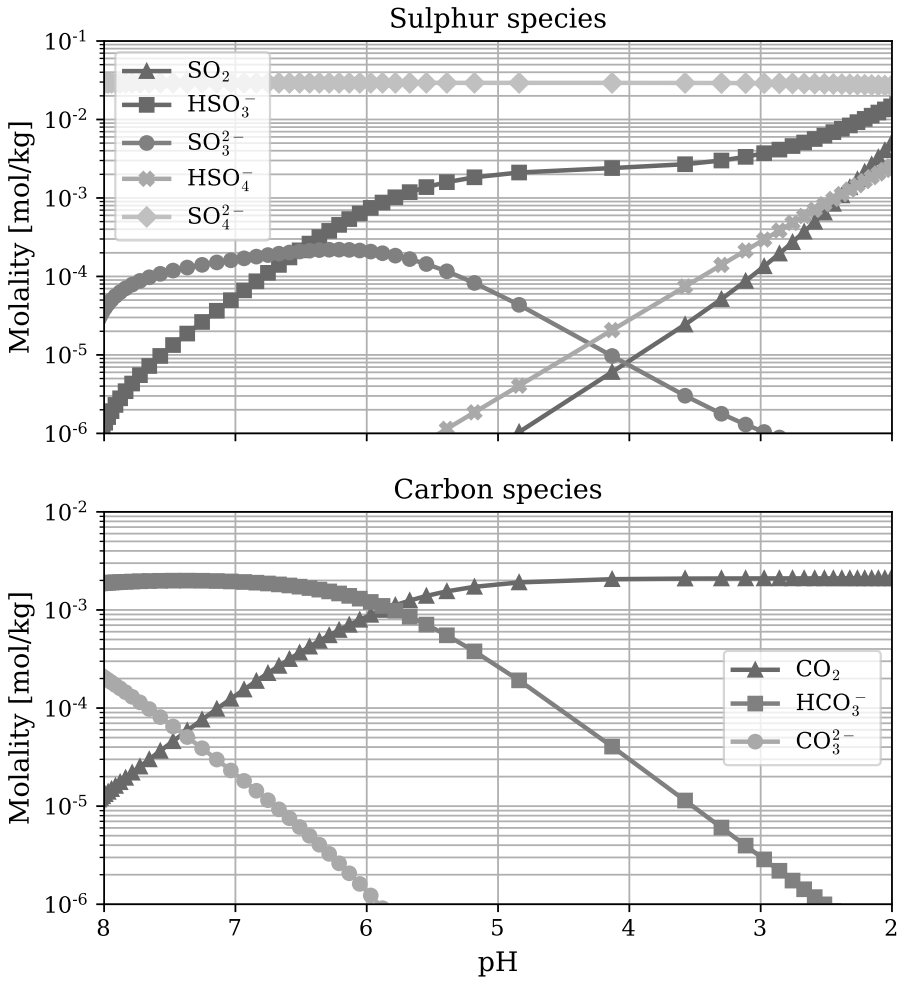

Fig. 3.3: Sulphur and carbon species molality during the acidification of seawater.

Finally, it can be noted that little change can be seen for the sulphate species, where the concentration of SO_4^{2-} remains almost unchanged until a pH of 3 is reached. Even though the change is relatively insignificant, the role of this equilibria in the model becomes apparent when oxidation of the sulphite species are considered.

3.1 Sulphite Oxidation

During the scrubbing process the sulphite species, that is HSO_3^-, and SO_3^{2-}, react with the oxygen in the liquid to produce sulphate species, HSO_4^-, and

SO_4^{2-}. The oxidation rate for the sulphite species can be given as follows [33]:

$$-\frac{d\left[\mathrm{S(IV)}\right]}{dt} = k'\left[\mathrm{S(IV)}\right]^2\left[\mathrm{O_2}\right]_l^{0.5} \tag{3.25}$$

Here the reaction rate is determined from the total concentration of sulphite species [S(IV)]. To express the reaction rate for the individual species the overall reaction rate is simply weighted by the fraction of concentration of the individual species to the concentration of the sulphites, which can be expressed as [33]:

$$\frac{d\left[\mathrm{HSO_3^-}\right]}{dt} = \frac{\left[\mathrm{HSO_3^-}\right]}{\left[\mathrm{S(IV)}\right]}\frac{d\left[\mathrm{S(IV)}\right]}{dt} \tag{3.26}$$

$$\frac{d\left[\mathrm{SO_3^{2-}}\right]}{dt} = \frac{\left[\mathrm{SO_3^{2-}}\right]}{\left[\mathrm{S(IV)}\right]}\frac{d\left[\mathrm{S(IV)}\right]}{dt} \tag{3.27}$$

The rate constant for the oxidation rate shown in equation 3.25, can be given as:

$$\log\left(k'\right) = \left(19.45 - \frac{5069.47}{T} + 14.74\sqrt{I} - 2.93I - \frac{2877\sqrt{I}}{T}\right) \tag{3.28}$$

It should be noted that the expression given for the oxidation rate in equation 3.28 has units of $\mathrm{L^{1.5}\,mol^{-1.5}\,min^{-1}}$. Therefore the oxidation rate is calculated in molarity $\mathrm{mol\,m^{-3}}$, and converted to mass fractions before assignment in OpenFOAM. One of the more computationally expensive operations in the model is the transfer of species across the gas-liquid interface. To limit the number of species that has to be accounted for in this process the oxygen concentration in the liquid is assumed to be in equilibrium. The equilibrium between the exhaust gas and liquid is expressed through Henry's law which can be given as follows [34]:

$$\left[\mathrm{O_2}\right]_l = H^{cc}\left[\mathrm{O_2}\right]_g \tag{3.29}$$

Chapter 4

Population Balance Model

In this section an overview of the population balance model used to model droplets sizes is given. The population balance model is implemented in the model presented in paper D.

In the scrubber a variety of droplet sizes exists, not only due to different droplet sizes produced by the nozzles, but also due to interfacial interactions between the exhaust gas and seawater. There are generally two different methods for tracking droplet sizes in an Eulerian framework. One method is to sub-divide the liquid phase into separate sub-phases where each sub-phase is assigned a single droplet size. The second method is to assign series of fields to the liquid phase where each field represents a given droplet size.

Each of the two methods comes with pros and cons. In the case where sub-phases are used to represent the droplet sizes, the exact size of the droplet is used in all of the sub-models resulting in a more detailed picture of the gas and liquid interactions throughout the scrubber. The drawback with this method is that for each of the sub-phases a complete set of, momentum, energy, and species equations have to be solved at each iteration, which is computationally expensive. In the case where a series of fields are used, a transport equation per field is required to be solved at each iteration, which is computationally cheaper compared to using sub-phases. A drawback is that an averaged droplet size have to be used for other sub-models such as drag or heat- and mass transfer.

Because the sub-phase method quickly becomes computationally expensive, as series of fields are used to represent the distribution of droplet sizes. To keep track of the droplet sizes and how the distribution changes throughout the scrubber the population balance model implemented in the OpenFOAM library is used [20]. The population balance model couples the transport equation for a given droplet size with events such as breakup, coalescence, drift, and nucleation, where the last two phenomena relates mainly to

bubbles.

Solving for the droplet sizes over a continuum is infeasible, and therefore the space of droplet sizes are discretised [35]. For the discrete equations, a range of droplet sizes over which the population balance model operates have to be defined and divided into a number of bins which represents the individual droplet size. Each bin has three main properties which are droplet diameter d_i, representative volume $x_i = \pi d_i^3/6$ and volume fraction f_i. The volume fraction defined such that the summation over all bins equals unity. [20].

As explained previously, an average droplet size has to be determined for liquid phase, in this case the Sauter mean diameter is used to represent the droplet size and can be given as:

$$d_{32} = 6 \left(\sum_{i=0}^{n_{bin}} \frac{a_i f_i}{x_i} \right)^{-1} \tag{4.1}$$

For the population balance model used in this work, it is assumed that droplet coalescence can be neglected, thus resulting in droplet breakup being the only phenomenon considered. With this assumption the transport equation for a single bin can be given as follows [20] :

$$\frac{\partial(\alpha_l f_i)}{\partial t} + \nabla \left(\alpha_l \vec{u}_l f_i \right) = \alpha_l \frac{f_i}{x_i} \sum_{j=i}^{n_{bin}} x_j n_{i,j} \Gamma_j - \alpha_l \Gamma_i f_i \tag{4.2}$$

where Γ_i is the breakup frequency of the droplet size under consideration, Γ_j is the breakup frequency of a droplet size larger than the droplet size under consideration, and $n_{i,j}$ is the fraction of droplets birthed by the breakup of a bin larger than the one under consideration.

In order to close the transport equation the breakup frequency, Γ and the fraction of droplets from breakup $n_{i,j}$. When determining $n_{i,j}$ probability distribution is used, which is called that daughter size distribution. In the following the derivation of these two parameters are explained.

1 Breakup Frequency

When droplets break it is caused by an external shear stress which overcomes the force of the surface tension trying to maintain the droplet shape. In the breakup model used in this work, two phenomena are considered for producing the external shear stress are turbulent induced shear stress and drag induced shear stress [36].

To determine when droplet breakup occur the Weber number is used as it relates the shear stress to the surface stresses created by the surface tension.

The Weber number can be expressed as:

$$We = \frac{\tau_i}{\tau_s} \tag{4.3}$$

where τ_i is the shear stress caused turbulence or drag, and τ_s is the surface stress caused by the surface tension. The surface stress can produced by the surface tension can be given as:

$$\tau_s = \frac{\sigma}{d} \tag{4.4}$$

When the Weber number exceeds a critical value breakup of the droplet occurs. The critical Weber number has been correlated to experimental work and can be given as [37]:

$$We_{cr} = \begin{cases} 55\left(\frac{24}{Re_d} + \frac{20.1707}{Re_d^{0.615}} - \frac{16}{Re_d^{2/3}}\right) & 200 < Re_d < 2000 \\ 5.48 & Re_d \geq 2000 \end{cases} \tag{4.5}$$

1.1 Turbulent Induced Breakup

The turbulent shear stress is derived based on the assumption of isotropic turbulence and can be given as [36]:

$$\tau_t = \left(\rho_l - \rho_g\right)\left(\frac{\rho_l}{\rho_g}\right)^{-1/3} \beta\left(\varepsilon d\right)^{2/3} \tag{4.6}$$

where ε is the turbulent dissipation rate and the model constant $\beta = 8.2$ [36].

As the turbulence model used in this work is the k-ω SST model, the turbulent dissipation rate, ε has to be calculated from the values of k and ω which can be given as follows [20]:

$$\varepsilon = \beta^* \cdot k\omega \tag{4.7}$$

where the model constant $\beta^* = 0.09$ [38].

Combining the expression for the turbulent shear stress presented in equation 4.6, Weber number presented in equation 4.3, and critical Weber number presented in equation 4.5, the critical diameter for the turbulent breakup can be determined as follows [36]:

$$d_{cr,t} = \left(\frac{We_{cr}\sigma}{\beta\left(\rho_l - \rho_g\right)}\right)^{3/5}\left(\frac{\rho_l}{\rho_g}\right)^{1/5} \varepsilon^{-2/5} \tag{4.8}$$

Lastly the turbulent droplet breakup time can be given as [36]:

$$t_{br,t} = \left(\varepsilon\frac{\rho_l}{\rho_g}\right)^{-1/3}\left(\beta\frac{\rho_l - \rho_g}{\rho_l}\right)^{-1/2} d^{2/3} \tag{4.9}$$

1.2 Drag Induced Breakup

For the drag induced droplet breakup the shear stress is based on the relative velocity between the droplet and the surrounding gas, which can be given as:

$$\tau_d = \rho_g \left(\left| \vec{u}_g - \vec{u}_l \right| \right)^2 \tag{4.10}$$

In the same manner as for the critical diameter for turbulent induced breakup, the critical diameter for drag induced breakup can be written as [36]:

$$d_{cr,d} = \frac{We_{cr}\sigma}{\rho_g \left(\left| \vec{u}_g - \vec{u}_l \right| \right)^2} \tag{4.11}$$

Finally the droplet breakup time can be determined as [36, 39]:

$$t_{br,d} = t^*_{br,d} \frac{d}{\left| \vec{u}_g \right|} \sqrt{\frac{\rho_l}{\rho_g}} \tag{4.12}$$

$$t^*_{br,d} = c \left(We_{cr} - 12 \right)^m \tag{4.13}$$

where $t^*_{br,d}$ is the dimensionless breakup time.

The coefficients c and m in equation 4.13 are dependent on the critical Weber number We_{cr}, and their values for all Weber numbers are presented in table 4.1:

c	m	We_{low}	We_{high}
7.00	0.00	1	12
6.00	-0.25	12	18
2.45	0.25	18	45
14.1	-0.25	45	351
0.766	0.25	351	2670
5.50	0.00	2670	∞

Table 4.1: Coefficients for dimension less breakup time, presented in equation 4.13 [39].

When the critical diameter, d_{cr} and breakup time t_{br} have been determined for both drag and turbulence the breakup frequency can be determined where the input to the function depends on which of the two phe-

nomena result in the smaller critical diameter:

$$\Gamma = \begin{cases} \frac{\left(\left(\frac{d}{d_{cr,t}}\right)^3 - 1\right)}{t_{br,t}} & d_{cr,t} < d_{cr,d} \\ \frac{\left(\left(\frac{d}{d_{cr,d}}\right)^3 - 1\right)}{t_{br,d}} & d_{cr,d} < d_{cd,t} \end{cases} \tag{4.14}$$

In figure 4.1 the critical diameter and breakup time for both drag and turbulence induced breakup are shown over a range of droplet diameters corresponding to that used in the model. For the case shown, it can be seen for droplets with a diameter below 0.7 mm that the smallest critical diameter results from turbulence while above it is drag that governs the breakup of the droplets. Examining the breakup time presented, it can be seen that the breakup occurs faster when it is induced by turbulence as compared to drag for droplets with a diameter below 0.75 mm.

This is of course not always the case, as an increase in the turbulent dissipation rate ε, reduces both the critical diameter and the turbulent breakup time for turbulence induced breakup. On the other hand if the relative velocity between the droplet and gas increases the drag induced breakup becomes dominant as the critical diameter is reduced. Even though the relative velocity also affect the breakup time its impact is almost neglectable compared to the velocity of the gas.

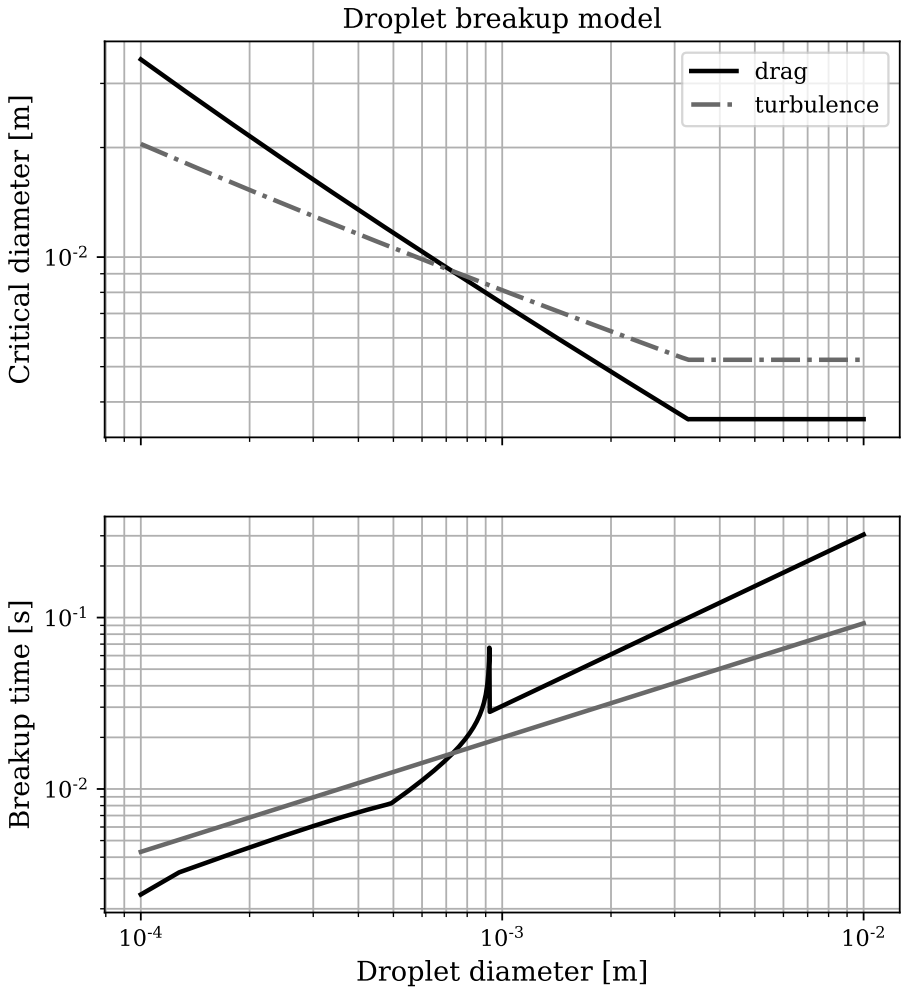

Fig. 4.1: Critical diameter and breakup time for turbulent and drag induced breakup. For the case depicted the following parameters are used: $\varepsilon = 5\mathrm{m}^2\,\mathrm{s}^{-3}$, $\sigma = 0.075\mathrm{N}\,\mathrm{m}^{-1}$, $|\vec{u}| = 7\mathrm{m}\,\mathrm{s}^{-1}$ and $|\vec{u}_g - \vec{u}_l| = 10\mathrm{m}\,\mathrm{s}^{-1}$, while the phase properties are that of seawater and exhaust gas at 298.15K.

2 Daughter Size Distribution

The daughter size distribution governs how volumes of the droplets resulting from a breakup are distributed. Because population balance models have been used extensively in the study of bubbles, there are several daughter size distributions available to characterise the breakup of bubbles. These models can be divided into three categories which are empirical, phenomenological

and statistical [40]. Because daughter size distributions are not readily available for droplet breakup a statistical model is used. Some of the statistical models for binary bubble breakup are presented in figure 4.2:

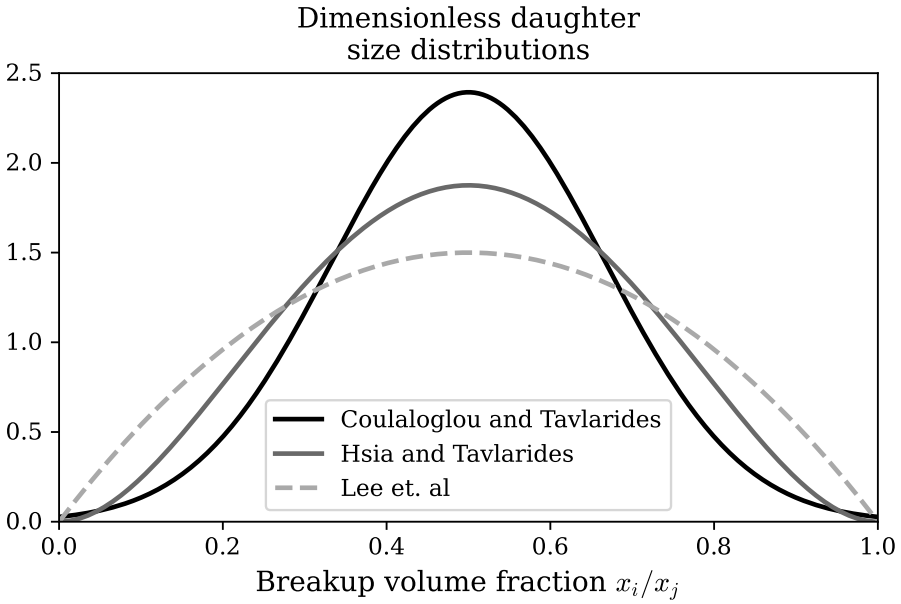

Fig. 4.2: Statistical daughter size distributions presented in the works of Coulaloglou and Tavlarides [41], Hsia and Tavlarides [42], and Lee et. al [43].

Common for all of the statistical daughter size distributions shown in figure 4.2 is that they are all centred around half the volume of the droplet breaking. Additionally all of the distributions are determined on the interval going from 0 to the size of the breaking droplet, which increases the probability of uneven breakage of the droplet.

By assuming that the breakup is binary and results in two droplet of approximately the same size, the daughter size distribution can be treated as a normal distribution. The distribution used in this work has mean of half the volume of the breaking droplet and a standard deviation equal 10% of the mean, this can be expressed as follows [44]:

$$\beta(x_i, x_j) = \frac{2}{0.1x_j\sqrt{2\pi}} \exp\left(-\frac{1}{2}\left(\frac{2x_i - x_j}{0.1x_j}\right)^2\right) \tag{4.15}$$

The number fraction $n_{i,j}$ is defined such that when a daughter droplet is formed and does not correspond to the representative volume of a bin, it is assigned to the adjoining bins. This results in following expression for

$n_{i,j}$ [35]:

$$n_{i,j} = \int_{x_i}^{x_{i+1}} \frac{x_{i+1} - v}{x_{i+1} - x_i} \beta\left(v, x_j\right) \mathrm{d}v + \int_{x_i}^{x_{i+1}} \frac{v - x_{i-1}}{x_i - x_{i-1}} \beta\left(v, x_j\right) \mathrm{d}v \tag{4.16}$$

3 Constraints And Stability

The final consideration for the population balance model is how the packed bed is represented. Clearly the concept of dispersed droplets is meaningless in this region of the scrubber due to the chaotic nature of the two-phase flow interacting with the random packing material. The discontinuity in the transport equations for the droplet sizes caused by the packed bed means that a distribution of droplet sizes have to be established at the bottom of the packed bed where the flow is again considered as dispersed droplets. Determining such a distribution for liquid droplet would require significant experimental efforts or high fidelity simulations, which is beyond the scope of this work. Here it is simply assumed that the droplet leaves bed with a uniform distribution with a diameter of 0.01m. The merit for such an assumption lies in observations made at a visit to laboratory that made analysis of pressure loss over the packing material. This assumption also allows for a way to handle the discontinuity caused by the packing material as it is simply to constrain the equation sets for all cells that are placed in the packed bed area in such a way that the droplet diameter is equal to 0.01m for the entire packed bed.

As it was shown in the section 1 the breakup frequency is dependent on both turbulence parameters of the k-ω SST model. This was found to result in instabilities when the liquid volume fraction approached unity because the system of equations for the turbulence model becomes numerically unstable when the gas volume fraction approaches zero. Therefore to improve the stability of the CFD-solver breakup is disabled in cells with a liquid volume fraction larger than 0.9. This cut-off is chosen arbitrarily as it simply made the solver progress. However, this value is still well above any point where the droplets would be considered to be dispersed.

Chapter 5

Interfacial Forces

In this section an overview of the interfacial forces used for the scrubber model in paper D are presented. In paper B a detailed description of the model used to describe the interfacial forces in the packed bed [45].

1 Dispersed Droplet Drag

With the variation of droplets sizes in the scrubber and varying velocities of both the gas and droplets a drag correlation which is valid over at large range of Reynolds numbers is used. The drag correlation, shown in equation 5.1, is based on measurements on spherical droplets, which is assumed to be valid for the droplets in the scrubber [46].

$$C_d = \left(\left(\frac{24}{Re_d} \right)^{0.52} + 0.32^{0.52} \right)^{1/0.52} \qquad 1 < Re_d < 10.000 \tag{5.1}$$

The droplet Reynolds number is given as follows:

$$Re_d = \frac{d\rho_g \left| \vec{u}_g - \vec{u}_l \right|}{\mu_g} \tag{5.2}$$

where d is the droplet diameter

The drag correlation for the droplets can be seen in figure 5.1:

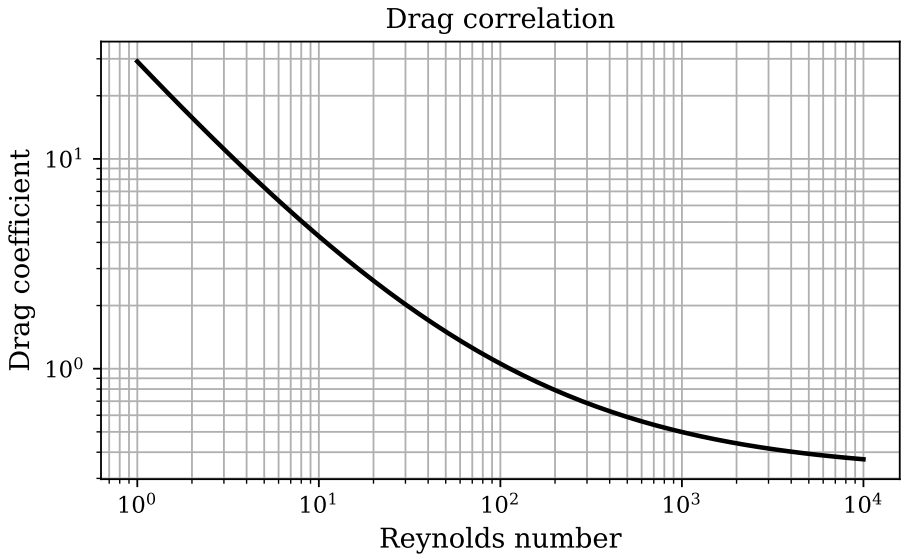

Fig. 5.1: Drag coefficient for dispersed droplets [46].

2 Packed Bed Force

The interfacial forces in the packed bed are modelled using a porous medium approach. There are several models presented in the literature for porous medium approaches in regards to random- and structured packing [47–49]. A method based on simplified momentum equations for determining the coefficients from experimental data was used and it was found that all of the models found in literature had issues with their predictive performance when used for the IMTP type packing used in the scrubber [45, 50]. (see paper B.)

The porous medium model accounts for three interaction forces that are gas-solid, liquid-solid, and gas-liquid. The three interaction forces can be expressed as [45]:

$$\vec{F}_{gs} = \alpha_g \left(\mathscr{A}_{gs} \mu_g + \mathscr{B}_{gs} \rho_g \left| \vec{u}_g \right| \right) \vec{u}_g \tag{5.3}$$

$$\vec{F}_{ls} = \alpha_l \left(\mathscr{A}_{ls} \mu_l + \frac{\mathscr{B}_{ls}}{\alpha_l^2} \rho_l \left| \vec{u}_l \right| \right) \vec{u}_l \tag{5.4}$$

$$\vec{F}_{gl} = \frac{\mathscr{A}_{gl} \left| \vec{u}_l \right| + \mathscr{B}_{gl} \left| \vec{u}_l \right|^2}{\left| \vec{u}_g - \vec{u}_l \right|} \left(\vec{u}_g - \vec{u}_l \right) \tag{5.5}$$

It should be noted that the expression used for the gas-liquid interaction force, shown in equation 5.5 differs from that presented in literature as the packing packing material used there is IMTP-50 and not IMTP-60 [45].

The coefficients $\mathscr{A}_{gs}$, $\mathscr{B}_{gs}$, $\mathscr{A}_{ls}$, $\mathscr{B}_{ls}$, $\mathscr{A}_{gl}$ and $\mathscr{B}_{gl}$ are determined from data from SULCOL 3.4.4, which is a proprietary software provided by the manufacture [51]. Because the data provided is proprietary the values of the coefficients cannot be presented here.

A comparison of the normalised pressure loss predicted by the porosity model and the normalised pressure loss from SULCOL 3.4.4 is shown in figure 5.2:

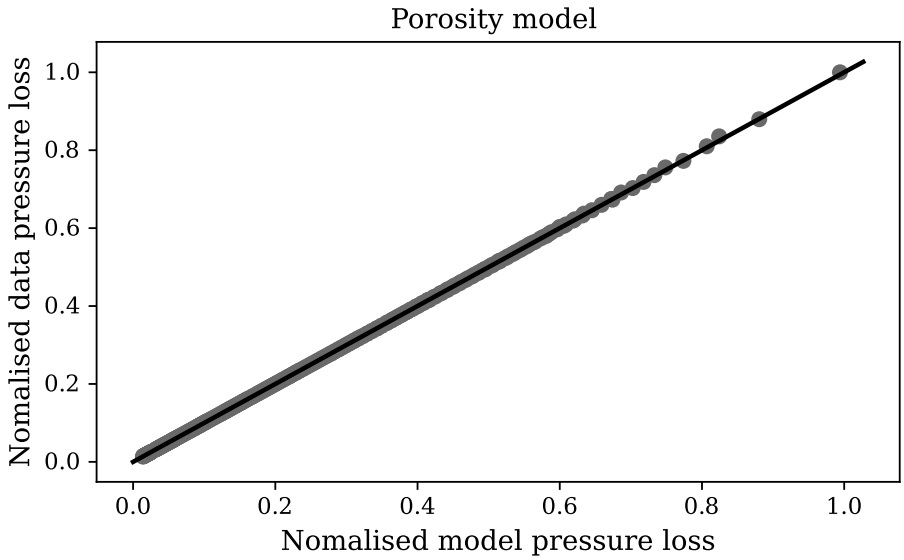

Fig. 5.2: Comparison of the porous medium model with data from SULCOL 3.4.4 [51].

3 Dispersion Force

When the seawater flows through the packed bed the impact on the surfaces of the random packing causes the seawater to spread out. This will occur until an equilibrum is reached, meaning that the liquid volume fraction is uniform. This phenomena can be treated as a dispersion force acting on the seawater. A model for liquid dispersion in packed beds have been presented in the literature, where a dispersion force has been added to the momentum equations of the phases [52]. The model for the dispersion force is expressed in the same manner as gas-liquid and liquid-solid interfacial forces given in equation 5.4, but they are proportional to a drift velocity instead of the

velocity of the phases. The dispersion force for the individual phases can be given as follows [52]:

$$\vec{F}_{dis,l} = \alpha_l \left(\mathscr{A}_{ls}\mu_l + \frac{\mathscr{B}_{gls}}{\alpha_l^2}\rho_l \left|\vec{u}_l\right| \right) \vec{u}_{d,l} + \left(\frac{\mathscr{A}_{gl}\left|\vec{u}_l\right| + \mathscr{B}_{gl}\left|\vec{u}_l\right|^2}{\left|\vec{u}_g - \vec{u}_l\right|} \right) \left(\vec{u}_{d,l} - \vec{u}_{d,g} \right) \tag{5.6}$$

$$\vec{F}_{dis,g} = \alpha_g \left(\mathscr{A}_{gs}\mu_g + \mathscr{B}_{gs}\rho_g \left|\vec{u}_g\right| \right) \vec{u}_{d,g} + \left(\frac{\mathscr{A}_{gl}\left|\vec{u}_l\right| + \mathscr{B}_{gl}\left|\vec{u}_l\right|^2}{\left|\vec{u}_g - \vec{u}_l\right|} \right) \left(\vec{u}_{d,g} - \vec{u}_{d,l} \right) \tag{5.7}$$

Where $\vec{u}_{d,g}$ and $\vec{u}_{d,l}$ are the drift velocity of gas and liquid phase, respectively.

The drift velocity for a phase is expressed in terms of the gradient of the volume fraction and velocity of the individual phase can be given as [52]:

$$\vec{u}_{d,i} = -\frac{D_s}{\alpha_i} \left(\left|\vec{u}_i\right| \nabla\alpha_i - \left(\vec{u}_i \cdot \nabla\alpha_i\right) \frac{\vec{u}_i}{\left|\vec{u}_i\right|} \right) \tag{5.8}$$

where D_s is the spread coefficient which is determined experimentally for the individual type of packing material.

Experiments for determining the spread coefficient in the IMTP packing material can be found in literature [53]. Here two methods for determining the spread coefficient were used. One is the central jet method, where a jet of water is injected at the top of a cylindrical packed bed and the distribution of water can then be measured at the bottom of the packed bed. The other is a tracer method, where a uniform flow is first established across the packed bed, then a tracer is injected in the same manner as the jet, and again collected at the bottom of the packed bed where the distribution can be determined. The spread coefficients found the IMTP type packing are shown below [53]:

	$D_s \times 10^{-3}$ m		
packing type	Jet	Tracer	mean
IMTP-40	2.45	2.95	2.7
IMTP-50	3.00	3.14	3.07
IMTP-60	4.09	4.20	4.145

Table 5.1: Spread coefficients for IMTP [53].

It can be noted that the spread coefficient for IMTP-60 which is used in the scrubber, are not reported. Therefore the value is interpolated using the mean values presented in table 5.1. This results in a spread coefficient for IMTP-60 $D_s = 3.61 \times 10^{-3}$m.

However it was discovered that when the dispersion model was implemented, as presented in equations 5.6, 5.7, and 5.8, there was little to no difference in the liquid distribution in the bed before and after the implementation.

To be able to determine what causes the lack of dispersion, the method for determining the spread coefficient D_s was further studied. When the spread coefficient is determined from experimental data gathered using the central jet method, the following differential equation is solved, where D_s calibrated to fit the solution to the data:

$$\frac{\partial L}{\partial h} = D_s \left(\frac{1}{r} \frac{\partial L}{\partial r} + \frac{\partial^2 L}{\partial r^2} \right) \tag{5.9}$$

Where L is the superficial velocity of the liquid, D_s is the spreading coefficient, r is the radial coordinate and h is the vertical coordinate.

Analytical solutions to equation 5.9 are presented in the literature, where different liquid distributors are considered [54]. Among the liquid distributors that are presented, the jet method is represented as a single point in the centre of a cylindrical bed. The solution corresponding to this boundary condition can be given as [54]:

$$L(r,h) = \frac{\dot{V}}{\pi R^2} + \frac{\dot{V}}{\pi R^2} \sum_{s=1}^{\infty} \frac{J_0\left(q_s r/R\right)}{J_0\left(q_s\right)^2} \exp\left(\frac{-q_s D_s h}{R^2} \right) \tag{5.10}$$

Where $\dot{V}$ is the volumetric flow from the source point, R is the radius of the column, J_0 is the Bessel of the 0^{th} order, and q_s is the roots to the derivative of J_0.

Comparing the solution of equation 5.10 with the results of the model, as presented in the literature, are shown in figure 5.3. Here it can be seen that in the centre of the column there is aprroximately an order of maginutude in difference in the superficial liquid velocity.

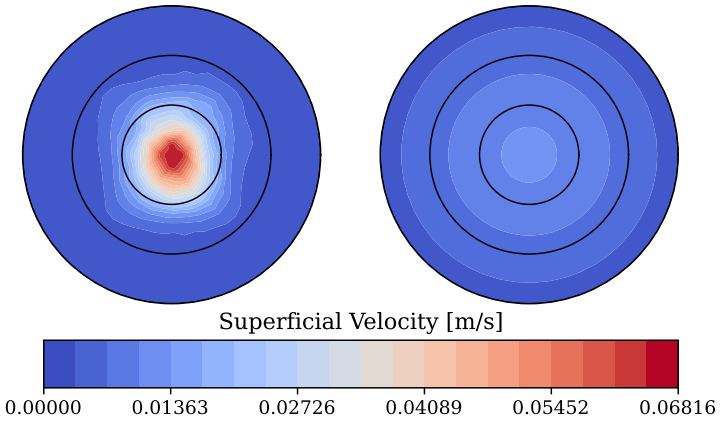

Fig. 5.3: Comparison of superficial liquid velocity 1 m from the jet, for the dispersion model presented in literature and analytical solution presented in equation 5.10 [52].The radial lines shown are spaced 0.05 m apart.

In a first attempt to match the results of the implemented model and the analytical solution, the value of D_s was increased in order to increase the dispersion force. This did however prove unsuccessful, as numerical instabilities quickly resulted in the CFD-solver not working. This was found to be caused by the fact that the volume fraction of the phases cancels out for the gas-solid and liquid-solid part for equations 5.6 and 5.7 when combining them with the drift velocity as presented in equation 5.8. This results in the dispersion force not being scaled properly when applied to the respective phases, which makes the system of equations used by the CFD-solver unstable.

To rectify this issue, the expression for the drift velocity is modified such that the volume fractions no longer cancels when combining equations 5.6, 5.7 and 5.8. The new expression for the drift velocity of the phases are given as [44]:

$$\vec{u}_{d_i} = F_s \left(|\vec{u}_i| \nabla \alpha_i - (\vec{u}_i \cdot \nabla \alpha_i) \frac{\vec{u}_i}{|\vec{u}_i|} \right) \tag{5.11}$$

where F_s is a spread factor.

The spread factor introduced in equation 5.11 is then calibrated such that the results of the implemented dispersion model matches that produced by the analytical solution. This is achieved by sweeping over a series of values for the spread factor and evaluating error between the averaged radial superficial velocity and the analytical solution. Here it was found that $F_s = 0.85$ resulted in the minimum error. In figure 5.4 contours of the modelled dispersion with the modified drift velocity and analytical solution are shown for varying distances from the jet.

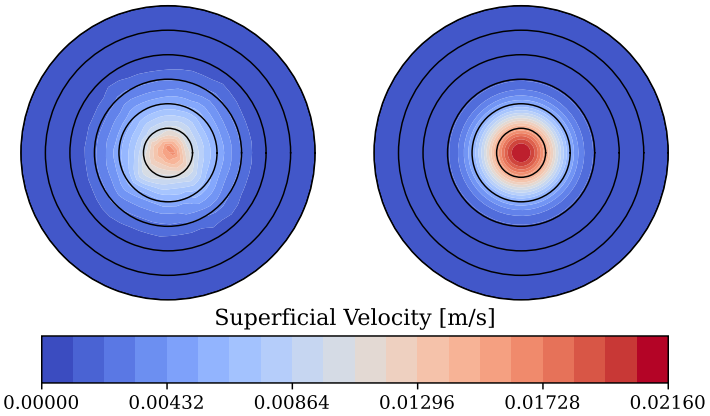

(a) Liquid superficial velocity 1 m from the jet.

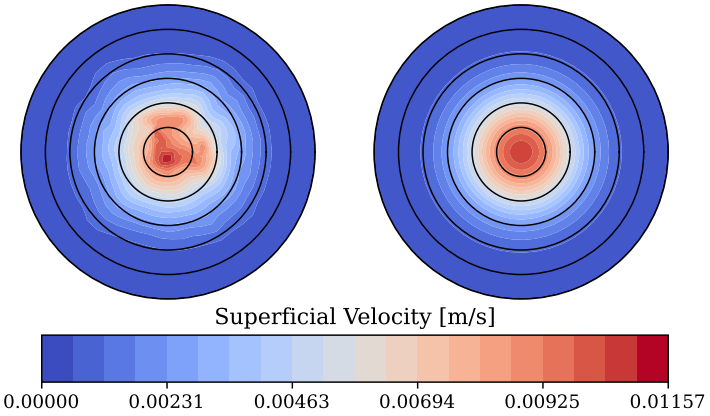

(b) Liquid superficial velocity 1.5 m from the jet.

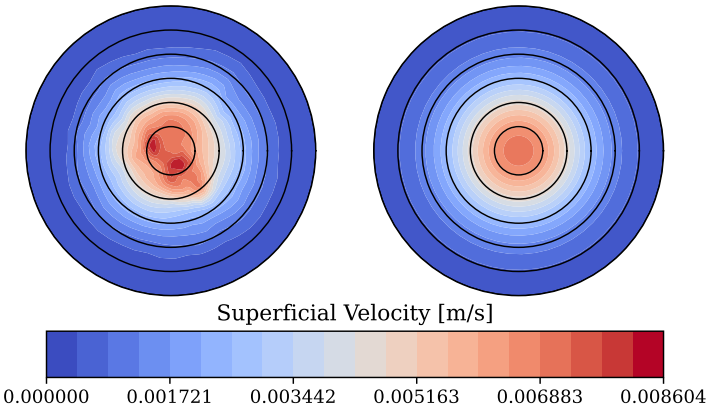

(c) Liquid superficial velocity 2 m from the jet.

Fig. 5.4: Liquid superficial velocity for the new dispersion model (on the left side) compared with the analytical solution (on the right side) for the dispersion. The radial lines shown in each figure are spaced 0.05 m apart. It should be noted that the colour grading mapped differently for each figure.

Chapter 6

Heat- And Mass Transfer

This section provides an overview of the heat- and mass transfer correlations used in the model presented in paper D. Furthermore, the correlations that will be presented for the internal heat- and mass transfer are detailed in Paper A [55].

The overall heat- and mass transfer coefficients do not depend on whether the region under consideration is dispersed droplet or packed bed as it is based on two phase film theory [20, 56]. The overall mass transfer coefficient can be given as:

$$\dot{m}_{gl,k} = \frac{\rho_g h_{g,k}\, \rho_l h_{l,k}}{\phi_k \rho_g h_{g,k} + \rho_l h_{l,k}} \left(Y_{g,k} - \phi_k Y_{l,k} \right) \tag{6.1}$$

$$\phi_k = \frac{\rho_l}{\rho_g H_k^{cc}}$$

where $h_{g,k}$ and $h_{l,k}$ are the mass transfer coefficient species k on the gas and liquid side of the interface, respectively. H_k^{cc} is the dimensionless Henry solubility for species k.

The Henry solubility H_k^{cc} is determined from the The van't Hoff equation which can be given as [34]:

$$H_k^{cc} = \frac{H^{cp\ominus}}{RT} \exp\left(\left(\frac{-\Delta_{sol} H}{R} + T \right) \left(\frac{1}{T} - \frac{1}{T^{\ominus}} \right) \right) \tag{6.2}$$

Where $H^{cp\ominus}$ is the concentration Henry solubility at standard temperature, R is the universal gas constant, and $\Delta_{sol} H$ is the enthalpy of dissolution.

Values for $H^{cp\ominus}$ and $-\Delta_{sol} H/R$ can be found in literature for SO_2 and CO_2 which are the species considered at the gas-liquid interface. [34]

For the overall heat transfer coefficient the expression is simpler than that for mass transfer as it relates only to the phases. The overall heat transfer

coefficient can be given as [20]:

$$\dot{Q}_{gl} = \frac{K_g K_l}{K_g + K_l}(T_g - T_l) \tag{6.3}$$

The difference between the two regions lies in how the heat- and mass transfer coefficients are expressed on each side of the interface. In this work the Chilton-Colburn analogy is assumed to be valid meaning that the mechanisms of heat and mass transfer are the same [56]. The analogy is used for the liquid side in droplet region and in both gas and liquid side in the random packing.

1 Dispersed Droplet Heat- And Mass Transfer

In the region with dispersed droplets the volumetric heat- and mass transfer coefficients on either side of the gas-liquid interface can be given as follows [20]:

$$h_{i,k} = \frac{6\alpha_l D_{i,k}}{d^2} Sh_{i,k} \tag{6.4}$$

$$K_i = \frac{6\alpha_l \kappa_i}{d^2} Nu_i \tag{6.5}$$

where $D_{i,k}$ is the diffusion coefficient of species k in phase i, $Sh_{i,k}$ is the Sherwood number, κ_i is the thermal conductivity of phase i and Nu_i is the Nusselt number.

On the gas side of the droplet interface two different correlations are used for the heat- and mass transfer. For the heat transfer coefficient the following correlation have been derived for spheres [57]:

$$Nu_g = 2 + 0.775 Re_d^{0.5} \frac{Pr^{1/3}/\sqrt{2\gamma+1}}{\left[1 + \left(\frac{1}{(2\gamma+1)^3 Pr}\right)\right]^{1/6}} \tag{6.6}$$

$$\gamma = \frac{1}{(1 + Re_d)^{0.25}}$$

For the mass transfer coefficient on the gas side the following expression is used [58]:

$$Sh_{g,k} = 2 + 0.552 {Re_d}^{1/2} Sc_k^{1/3} \tag{6.7}$$

On the liquid side of the droplets gas-liquid interface a heat- and mass transfer model was developed in paper A. This model is based on internal circulation for droplet for low and high Reynolds numbers, where a different

set of streamlines are used depending on the case. The streamlines used for the low and high Reynolds number cases are shown in figure 6.1:

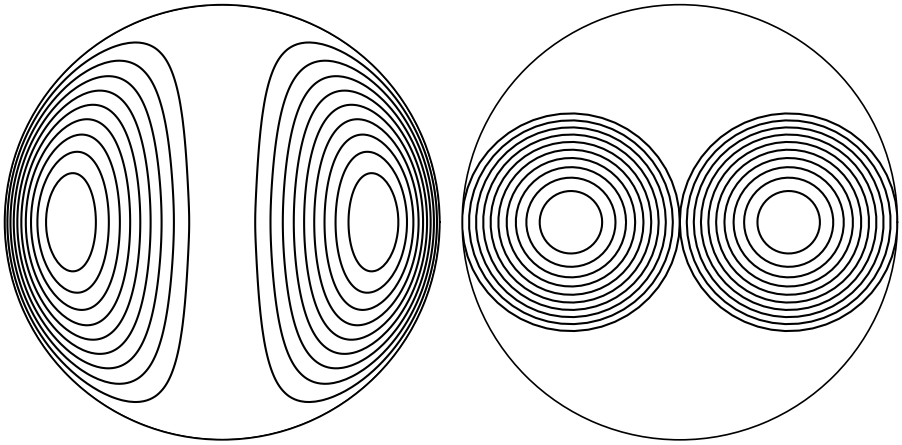

Fig. 6.1: Streamlines for the internal circulation in droplets for low and high Reynolds numbers [55]. The streamlines shown on the left hand side of the figure are used for the low Reynolds number case, while the streamlines on the right hand side are used for high Reynolds number case [59, 60].

In both cases, the transfer of heat and mass is a function of a modified Peclet number, which can be specified for each type of transfer as:

$$Pe_{m,k} = \frac{d\left|\vec{u}_g - \vec{u}_l\right|}{D_{l,k}} \tag{6.8}$$

$$Pe_{th} = \frac{d\left|\vec{u}_g - \vec{u}_l\right|}{\alpha_{th,l}} \tag{6.9}$$

$$Pe' = \frac{\mu_g}{\mu_g + \mu_l} Pe \tag{6.10}$$

For each case numerical simulations were carried out over a range of modified Peclet numbers and the Nusselt or Sherwood number determined for the individual Peclet number based on the averaged dimensionless temperature or mass concentration. From the results of the numerical simulations, a correlation between the modified Peclet number and the Nusselt or Sherwood number was made. For the low Reynolds number case the following correlation was determined [55]:

$$N_{t,low} = \begin{cases} a\left[1 - b \cdot \exp\left(-c \cdot Pe'\right) \sin\left(d \cdot Pe' + e\right)\right] + 7.551 & Pe' \leq 1000 \\ b \cdot \exp\left(-c \cdot Pe'\right) \sin\left(d \cdot Pe' - e\right) + 19.18 & Pe' > 1000 \end{cases} \tag{6.11}$$

Where $N_{t,low}$ is either the Nusselt or Sherwood number depending on which phenomenon is considered. The coefficients for the expressions presented in equation 6.11 are given in table 6.1 below:

Peclet number	a	b	c	d	e
$Pe' \leq 1000$	1.249×10^{1}	1.030	1.269×10^{-3}	5.169×10^{-3}	1.677
$Pe' > 1000$	-	3.013	5.149×10^{-4}	6.508×10^{-3}	2.575

Table 6.1: Coefficient for equation 6.11 [55].

For the high Reynolds number case the Nusselt or Sherwood were found to be a simple linear correlation that can be given as [55]

$$N_{t,high} = 1.523 \times 10^{-2} \cdot Pe' \tag{6.12}$$

Finally the model was compared to experimental data for heat transfer in free falling droplets, and it was found that the best results were achieved when switching between the low and high Reynolds number cases when the Reynolds number of the droplet exceeded 400. This gives the final expression for the heat- and mass transfer model, which is expressed as follows [55]:

$$N_t = \begin{cases} N_{t,low} & Re_d \leq 400 \\ N_{t,high} & Re_d > 400 \end{cases} \tag{6.13}$$

2 Packed Bed Heat- And Mass Transfer

A brief discussion of how heat and mass transfer coefficients for the packed bed are derived are given in paper D. This sub-section serves to give a better insight into its derivation.

Contrary to the heat and mass transfer coefficient for the dispersed droplets, the use of Nusselt and Sherwood numbers are not present in the correlations for the packed bed, where the heat and mass transfer coefficient are directly expressed instead.

The heat and mass transfer coefficients for the packed bed are based on an already existing model found in the literature [61]. However, the expression for the model presented has other correlations included for the volume fractions of the both phases, in addition to conversions from superficial velocities to interstitial which also involves volume fractions. Because these values are already available from the CFD-solver these correlations have to be substituted. In addition there is only presented mass transfer correlations in the

literature used for the model, so theses will have to be derived from the same starting point as the mass transfer coefficients.

The heat- and mass transfer coefficients are based on Higbies penetration theory [62]. Here it is assumed that the liquid forms a film on the surface of the packing material, where the contact time between the gas at the surface of the film is short enough for the bulk temperature or mass concentration to remain constant during the period. This is illustrated in figure 6.2:

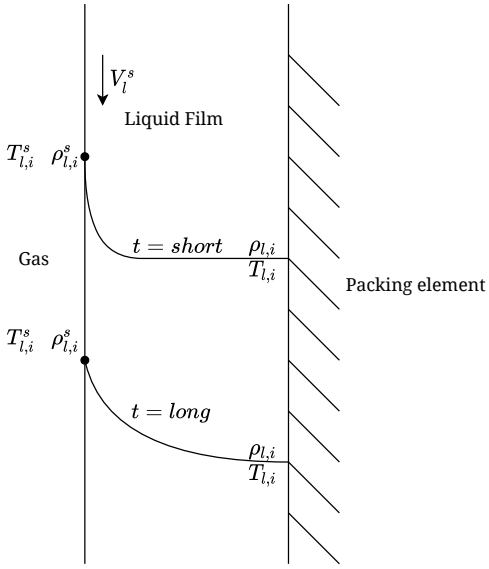

Fig. 6.2: Conceptual sketch of temperature or mass concentration profile for a liquid film on a packing element with short and long contact times.

This means that the liquid film can be treated as a semi-infinite medium where the transfer occurs through unsteady diffusion. This problem is well described and solutions for various boundary conditions are readily available [63]. Following the derivation of the existing model a constant temperature and mass concentration is assumed at the films surface during the contact time, which results in the following local heat and mass transfer coefficients on the surface of the film [64]:

$$K_l^A = \frac{\kappa_l}{\sqrt{\pi \alpha_{th,l} \tau_l}} \tag{6.14}$$

$$h_l^A = \sqrt{\frac{D}{\pi \tau_l}} \tag{6.15}$$

where K_l^A and h_l^A are the area based heat- and mass transfer coefficients, and

τ is the contact time.

By defining the contact τ as the time it takes the film to move some distance, and taking an integral average over the hydraulic diameter of a packing element the expression for the heat and mass transfer coefficients becomes [62, 64]:

$$K_l^A = \frac{2\kappa}{\sqrt{\pi}} \sqrt{\frac{|\vec{u}_l|}{\alpha_{th,l} d_h}} \tag{6.16}$$

$$h_l^A = \frac{2}{\sqrt{\pi}} \sqrt{\frac{D\,|\vec{u}_l|}{d_h}} \tag{6.17}$$

$$d_h = 4\frac{1-\alpha_s}{a_s} \tag{6.18}$$

where α_s is the volume fraction of the packing material and a_s is the specific surface area of the packing material.

In the existing model it is assumed that the gas side mass transfer also follows the law of unsteady diffusion, which means that the gas side expressions can be derived in the same manner as equations 6.16 and 6.17. However, it is recognised that other phenomena also governs the gas side mass transfer in the existing model, therefore effects of the Reynolds number and Schmidt number are included.

The final step before the volumetric heat- and mass transfer coefficients can be determined is to express the specific interfacial area between the gas and liquid in the packed bed. Here a correlation has been made in the same work as the existing mass transfer model. The correlation presented have been derived through dimensionless analysis for a large range of different packing materials and can be given as [61]:

$$a_{Ph} = 1.5a\,(ad_h)^{-0.5}\, Re_l^{-0.20} We_l^{0.75} Fr_l^{-0.45} \tag{6.19}$$

In the correlation for the specific interfacial area the dimensionless quantities are based on the hydraulic diameter of the packing material and the superficial velocity of the liquid.

By combining 6.16, 6.17 and 6.19 and collecting all constant terms into a packing specific parameter C_K or C_h the final expression can be given as [44, 64]:

$$K_l = C_{K,l}\kappa_l \sqrt{\frac{|\vec{u}_l|}{\alpha_{th,l} d_h}} a_{Ph} \tag{6.20}$$

$$h_{l,k} = C_{h,l} \sqrt{\frac{D_{l,k}\,|\vec{u}_l|}{d_h}} a_{Ph} \tag{6.21}$$

$$K_g = C_{K,g}\kappa_g \sqrt{\frac{|\vec{u}_g|}{\alpha_{th,g} d_h}}\, Re_g^{\frac{3}{4}}\, Pr_g^{\frac{1}{3}}\, a_{Ph} \tag{6.22}$$

$$h_{g,k} = C_{h,g} \sqrt{\frac{D_{g,k}\,|\vec{u}_g|}{d_h}}\, Re_g^{\frac{3}{4}}\, Sc_g^{\frac{1}{3}}\, a_{Ph} \tag{6.23}$$

These packing specific parameter C_K or C_h are unknown for the IMTP-60 packing used for the packed bed and have to be calibrated to data. This is one of the key outcomes of paper D and the results of the calibration are presented there.

Chapter 7

Boundary Conditions

In the scrubber there are several surface patches which requires boundary conditions to be prescribed, this includes the walls, nozzles, scrubber inlet and outlet, and the drain pipe for the seawater. For all outlets in the scrubber a zero gradient boundary condition is applied for all fields in the model and at the inlets all scalar fields have a uniform value. However determining these values does require attention to paid to their formulation.

In paper D a detailed description of the boundary conditions applied for velocity and volume fraction on the nozzle are given, while others are referenced or briefly described . This section serves to explain these in more detail.

1 Turbulence

For the $k\omega$-SST turbulence model used for the gas phase, the values of k and ω have to be determined at the inlet of the scrubber. The turbulent kinetic energy is determined from the turbulence intensity for a fully developed pipe flow, which can be given as follows [65]:

$$I_k = 0.16 Re_{dh}^{-1/8} \tag{7.1}$$

$$k_g = 1.5 \left(I_k \left| \vec{u}_g \right|_{avg} \right)^2 \tag{7.2}$$

where I_k is the turbulence intensity, Re_{dh} is the Reynolds number of the exhaust gas based on the hydraulic diameter of the inlet pipe, k_g is the turbulent kinetic energy, and $\left| \vec{u}_g \right|_{avg}$ is the average gas velocity at the inlet.

With k_g determined the specific dissipation rate can be determined from the turbulent length scale and the value of k_g at the inlet. The turbulent

length scale is also based on a fully developed pipe flow, where the length scale relates to the hydraulic diameter of the pipe. The turbulent length scale and specific dissipation rate can be given as [65]:

$$l_{dh} = 0.07 d_h \tag{7.3}$$

$$\omega_g = \frac{\sqrt{k_g}}{C_\mu l_{dh}} \tag{7.4}$$

For the walls a continuous wall function is used to describe the law of the wall, which can be given as [66]:

$$y^+ = u^+ + \frac{1}{E}\left(\exp(\kappa u^+) - 1 - \kappa u^+ - 0.5(\kappa u^+)^2 - \frac{1}{6}(\kappa u^+)^3\right) \tag{7.5}$$

where y^+ is the dimensionless wall distance, u^+ is the dimensionless velocity at the wall, κ is the von Kármán constant which is 0.41 and E is a model constant which is 9.8.

2 Scrubber Inlet Species

In paper D the data presented from the scrubber system aboard an ocean going vessel did not contain the concentration of SO_2 at the scrubber inlet. Therefore, it has to be calculated from the data that are available. As mentioned in section 1, the SO_2 concentration is reported in relations to the concentration of CO_2 at the outlet of the scrubber. Even though the carbonate species present in the seawater are converted to CO_2 as the seawater acidifies during the scrubbing process, as shown in section 3, the amount that is released into the exhaust gas stream is neglectable in comparison to the amount of CO_2 originating from the combustion of fuel oil. The CO_2 concentration can therefore be assumed to be constant throughout the scrubber, which is also accepted by the IMO [6]. With this assumption it is possible to calculate the concentration of SO_2 at the inlet of the scrubber if the composition of the elemental components in fuel oil is know, which is case here as it has been reported by ship owner.

To calculate the concentration of SO_2 at the inlet, the following reaction for stoichiometric combustion of a fuel oil, where the air is assumed to be dry and consisting only of oxygen and nitrogen, has to be solved:

$$\begin{aligned} &x_0\mathrm{C} + x_1\mathrm{H} + x_2\mathrm{O} + x_3\mathrm{N} + x_4\mathrm{S} + x_a\,(0.21\mathrm{O_2} + 0.79\mathrm{N_2}) \rightarrow \\ &y_0\mathrm{CO_2} + y_1\mathrm{H_2O} + y_2\mathrm{SO_2} + y_3\mathrm{N_2} \end{aligned} \tag{7.6}$$

where x_i is the molar fraction of the respective element in a mole of fuel, x_a is the number of moles of air required for stoichiometric combustion and y_i is number of moles of the respective combustion products.

Balancing the reaction in equation 7.6 results in the following matrix equation for stoichiometric combustion:

$$\begin{array}{c} \\ \mathrm{C} \\ \mathrm{H} \\ \mathrm{O} \\ \mathrm{N} \\ \mathrm{S} \end{array} \begin{array}{c} \begin{array}{ccccc} y_0 & y_1 & y_2 & y_3 & x_a \end{array} \\ \begin{bmatrix} 1 & 0 & 0 & 0 & 0 \\ 0 & 2 & 0 & 0 & 0 \\ 2 & 1 & 2 & 0 & -2 \cdot 0.21 \\ 0 & 0 & 0 & 2 & -2 \cdot 0.79 \\ 0 & 0 & 1 & 0 & 0 \end{bmatrix} \end{array} \begin{bmatrix} y_0 \\ y_1 \\ y_2 \\ y_3 \\ x_a \end{bmatrix} = \begin{bmatrix} x_0 \\ x_1 \\ x_2 \\ x_3 \\ x_4 \end{bmatrix} \tag{7.7}$$

The stoichiometric combustion results in a CO_2 concentration which is significantly larger than that seen at scrubber outlet. However, as internal combustion engines does not run on a stoichiometric fuel to air ratio, but rather a lean mixture, an excess air ratio is included into equation 7.6. As the excess air simply passes through the engine, $y0$, $y1$, and $y2$, remains the same and one only have to find the number of moles of N_2 and O_2 (which is now in excess and therefore part of the products) in the products. The number of moles of N_2 and O_2 in the combustion products with excess air can be given as:

$$y_3 = \frac{x_3}{2} + 0.79 x_a \lambda \tag{7.8}$$

$$y_4 = 0.21 \left(\lambda - 1\right) x_a \tag{7.9}$$

where λ is the excess air ratio and y_4 is the number of mole of oxygen in the combustion products.

Finally the mole fraction of CO_2 can be found, which corresponds to the volumetric fraction that is given in the data, assuming ideal gas behaviour. The mole fraction of CO_2 in the combustion products can be given as:

$$X_{CO_2} = y_0 \left(\sum_{i=0}^{5} y_i \right)^{-1} \tag{7.10}$$

The excess air coefficient can then be solved for using a least-squares method such that the CO_2 concentration matches that given in the data set.

In the data set presented in paper D the concentration is approximately 4.8% by volume which corresponds to an excess air ratio of 3.1, as shown in figure 7.1, which is the range normally seen on large marine engines. Additionally it can also be seen that the concentration of SO_2 is around 1300 ppm at a CO_2 concentration of 4.8% by volume.

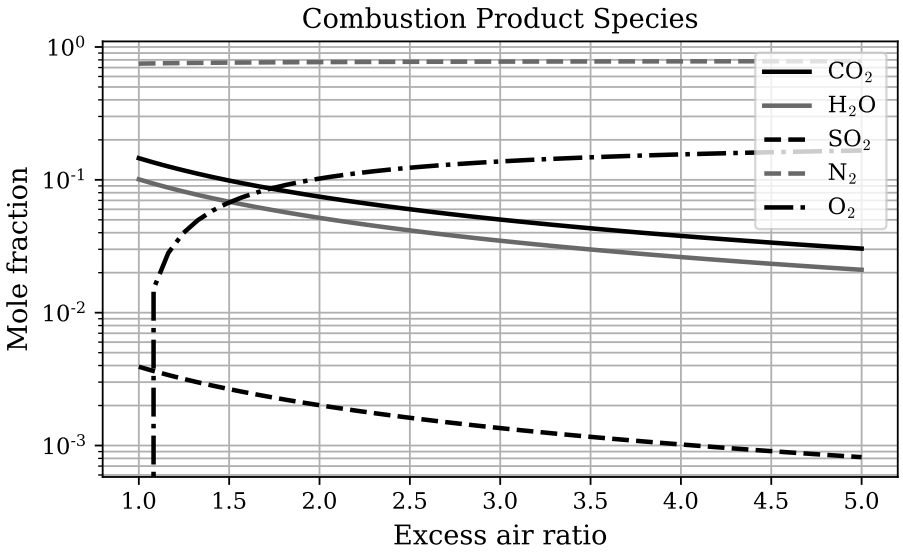

Fig. 7.1: Mole fractions of combustion product species with increasing excess air ratio.

Before the molar fractions of species that were found for the corresponding concentration of CO_2 can be implemented into the model, they have to be converted into mass fractions. The conversion from molar fractions to mass fractions can be given as follows:

$$Y_i = X_i MW_i \left(\sum_j X_j MW_j \right)^{-1} \tag{7.11}$$

3 Droplet Distribution

The three nozzle layers in the scrubber all have different orifice diameters and operate at different velocities. This results in the droplet distribution sizes to vary depending on the nozzle layer. To model droplet sizes originating from the the nozzles, the single-phase nozzle model is used [67]. Here the Sauter mean diameter can be given as [68]:

$$d_{32} = 133 \frac{d_n}{8} \left(\frac{\rho_l \left| \vec{u}_l \right|^2 d_n}{8\sigma_l} \right)^{-0.74} \tag{7.12}$$

where d_n is the diameter of the nozzle orifice and σ is the surface tension of the seawater.

The distribution of droplets is modelled using the Rosin-Rammler distribution is used, which can be given as [69]:

$$RR_{CDF} = \exp\left(-\left(\frac{d}{\bar{d}}\right)^{s}\right) \tag{7.13}$$

where d is the droplet diameter, $\bar{d}$ is the Rosin-Rammler diameter, and s is the spread factor of the distribution which is 3.5 for the single phase nozzle model [67].

Finally the Rosin-Rammler diameter has to be expressed in terms of the Sauter mean diameter which can be done as follows [69]:

$$\bar{d} = d_{32}\Gamma\left(1 - \frac{1}{s}\right) \tag{7.14}$$

where Γ is the Gamma functions.

The Rosin-Rammler distribution can then be used to set the boundary condition for population balance model at nozzle inlets by evaluating equation 7.13 at the boundaries of each bin in the population balance model. Distributions of the droplet diameters for the three nozzle layers in scrubber are shown in figure 7.2:

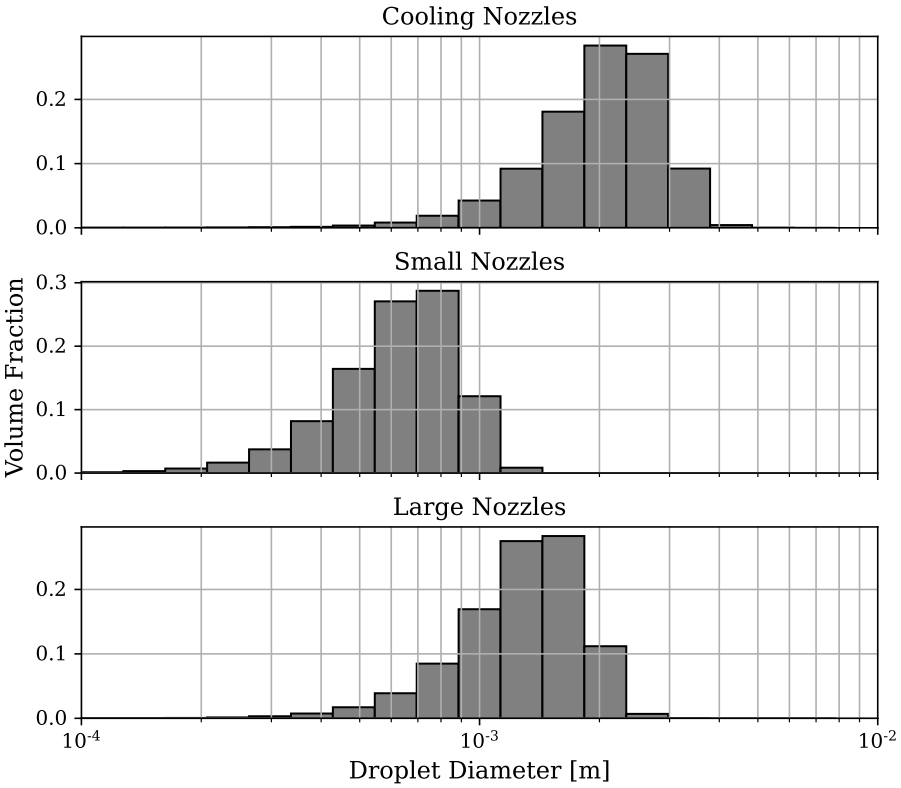

Fig. 7.2: Distribution of droplets for the three nozzle layers in the scrubber.

Chapter 8

Optimisation

In paper D, a gradient free optimisation method is used to calibrate the heat and transfer parameters for the packing. This method is the Efficient Global Optimisation method (EGO) [70], which uses a multivariate surrogate defined on a closed interval to perform the optimisation. The version of EGO used in this work is implemented in the optimisation package DAKOTA [71]. The following section serves as an outline of how the EGO works.

1 Gaussian Process

The surrogate used by EGO is a Gaussian Process Model (GP), which is a stochastic regression method. The model for the regression is simply a weighted sum linear and non-linear function that can be given as:

$$y\left(\mathbf{x^i}\right) = \sum_h \beta_h f_h\left(\mathbf{x^i}\right) + \varepsilon\left(\mathbf{x^i}\right) \tag{8.1}$$

The errors $\varepsilon\left(\mathbf{x^i}\right)$, between the observed value $y\left(\mathbf{x^i}\right)$, and the weighted functions are normally distributed with mean zero and variance σ^2.

The general idea behind GP is that the errors between the different observations $\varepsilon\left(\mathbf{x^i}\right)$ and $\varepsilon\left(\mathbf{x^j}\right)$ are not independent but correlated. The correlation between two points $\mathbf{x^i}$ and $\mathbf{x^j}$ is expressed based on distance, such that the smaller the distance is between the two points the more they are correlated. The correlation of each point can be put in a matrix $\mathbf{C}$, where the entries can be given as follows:

$$\mathbf{C_{i,j}} = \mathrm{Corr}\left[\varepsilon\left(\mathbf{x^i}\right), \varepsilon\left(\mathbf{x^j}\right)\right] = \exp\left(-\sum_{h=1}^{k} \theta_h \left|\mathbf{x^i} - \mathbf{x^j}\right|^2\right) \tag{8.2}$$

The summation in the exponential term of equation 8.2 account for the number of dimensions in a sample point $\mathbf{x}$. This means that a value θ_h has to be determined for each dimension of $\mathbf{x}$. θ_h determines how active the surrounding variables are at a given point and this can be seen in figure 8.1 where a heat map of the correlation matrix $\mathbf{C}$ is shown with two different values of θ_h. A lower value of θ_h corresponds to a wider area where correlation between the variables are high.

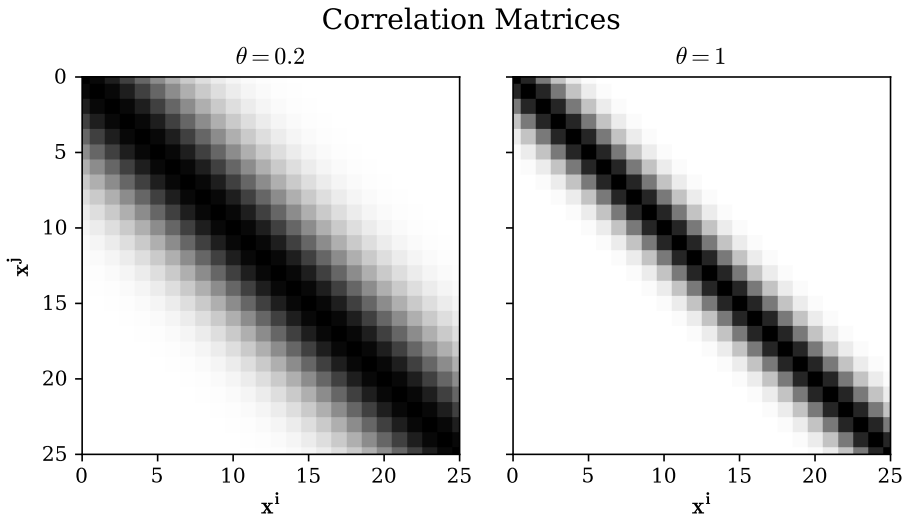

Fig. 8.1: Heat maps of the correlation correlation matrix for a one dimensional function. A darker colour corresponds to a higher value for the entry at $\mathbf{i}, \mathbf{j}$, which indicates a higher correlation between $\mathbf{x}^{\mathbf{i}}$ and $\mathbf{x}^{\mathbf{j}}$.

A major advantage of implementing the correlations as in equation 8.2 is that the weighted combination of the functions $\beta_h f_h\left(\mathbf{x}^{\mathbf{i}}\right)$ can be replaced by the means of the functions, resulting in:

$$y\left(\mathbf{x}^{\mathbf{i}}\right) = \mu + \varepsilon\left(\mathbf{x}^{\mathbf{i}}\right) \tag{8.3}$$

From here on the only parameters that are unknown are μ and variance σ^2 for $\varepsilon\left(\mathbf{x}^{\mathbf{i}}\right)$ which are both dependent on the parameter θ_h from equation 8.2. The expression for the regression given in equation 8.3, is now a multivariate normal distribution where the mean and variance can be found by maximising the log-likelihood. The log-likelihood is given in the following equation where constants and scaling terms are neglected as they have no impact on the evaluation of the maximum:

$$\ln \mathcal{L} = -\frac{n}{2} \ln \hat{\sigma}^2 - \frac{1}{2} \ln |\mathbf{C}| \tag{8.4}$$

The mean and variance can now be expressed for a set of sampled function values $\mathbf{y}$ with n samples where $\mathbf{1}$ is a vector of ones with length n:

$$\hat{\mu} = \frac{\mathbf{1}^{\mathrm{T}}\mathbf{C}^{-1}\mathbf{y}}{\mathbf{1}^{\mathrm{T}}\mathbf{C}^{-1}\mathbf{1}} \tag{8.5}$$

$$\hat{\sigma}^2 = \frac{(\mathbf{y} - \mathbf{1}\hat{\mu})^{\mathrm{T}}\,\mathbf{C}^{-1}\,(\mathbf{y} - \mathbf{1}\hat{\mu})}{n} \tag{8.6}$$

Combing equations 8.4, 8.5, and 8.6 the value for θ_h that maximises the log-likelihood can be found and the GP is ready to make predictions based on new points $\mathbf{x}^*$. When predicting the new function values a new correlation matrix $\mathbf{c}$ which gives the correlation between the new point and the sample points is required and can be given as in equation 8.2, which is expressed as follows:

$$\mathbf{c} = \mathrm{Corr}\left[\varepsilon\left(\mathbf{x}^*\right), \varepsilon\left(\mathbf{x}^{\mathbf{i}}\right)\right] \tag{8.7}$$

The correlation matrix between the new point and the sample points can then be used to find the function value, $\hat{f}\left(\mathbf{x}^*\right)$, and the variance, $\hat{\sigma}^2_*$, at the new point as follows:

$$\hat{f}\left(\mathbf{x}^*\right) = \hat{\mu} + \mathbf{c}^{\mathrm{T}}\mathbf{C}^{-1}\left(y - 1\hat{\mu}\right) \tag{8.8}$$

$$\hat{\sigma}^2_* = \hat{\sigma}^2\left(1 - \mathrm{diag}\left(\mathbf{c}^{\mathrm{T}}\mathbf{C}^{-1}\mathbf{c}\right)\right) \tag{8.9}$$

In figure 8.2 a GP is used to predict the response of some one dimensional function $f(x)$ on an interval of $x \in [0, 10]$ where five random samples have been drawn from the function. It can be seen that the variance at the sample points are zero while it increases as the distance between the sample point and x increases.

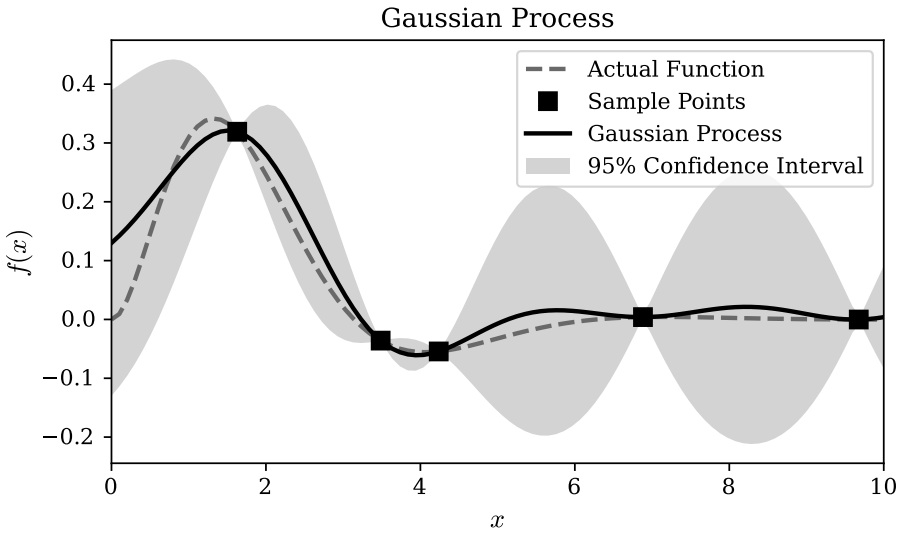

Fig. 8.2: Regression of a function using the Gaussian process.

2 Expected Improvement

Simply sampling the cost function of the optimisation problem and using GP to produce a response where the variance is sufficiently low everywhere is not very efficient, especially when dealing with expensive function evaluations. Therefore, an expected improvement function is used to determine where the next sample point should be taken. The expected improvement function weights the requirement for verification of local predictions; that is reducing the uncertainty of the GP around the current minimum, compared to exploring the remaining design space for other minima. The expected improvement can be given as follow:

$$EI\left(\mathbf{x}^*\right) = \left(f_{min} - \hat{f}\left(\mathbf{x}^*\right)\right)\Phi\left(\frac{f_{min} - \hat{f}\left(\mathbf{x}^*\right)}{\hat{\sigma}_*}\right) + \hat{\sigma}_*\phi\left(\frac{f_{min} - \hat{f}\left(\mathbf{x}^*\right)}{\hat{\sigma}_*}\right) \quad (8.10)$$

where f_{min} is the current minimum in the set of sampled function values, Φ and ϕ is the probability density function and the cumulative distribution function of the normal distribution, respectively.

In figure 8.3 the expected improvement for a GP is shown. For the case presented the expected improvement is weighted towards local exploration near the current minimum of the GP. Here it can be seen that the maximum of $EI(x)$ is at $x = 2.1$ where the GP has its current minimum which is between two sample points at $x = 1.4$ and $x = 2.6$. Another local maximum in $EI(x)$

can be seen $x = 5.7$. Even though the GP does not have a minima at this location the variance of the GP at this point is close to its maximum.

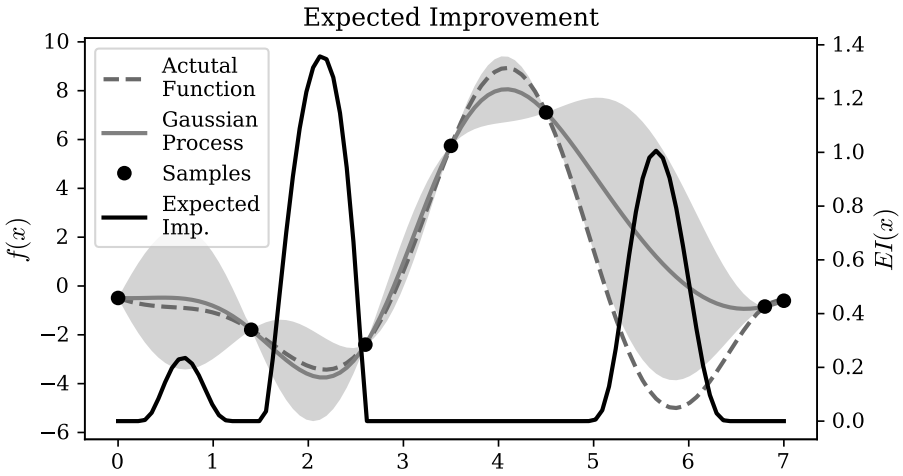

Fig. 8.3: Expected improvement function for a Gaussian process.

In practice finding the maximum of the expected improvement is done using a global optimisation method, which is computationally cheaper than evaluating $EI(x)$ over the entire design space. In the method implemented in DAKOTA the DIRECT optimisation method is used to maximise the expected improvement function [71, 72].

3 Efficient Global Optimisation Algorithm

To initialise the EGO a set of samples has to be taken from the cost function. The sample points are generated using a Latin Hypercube Sampling to ensure that the interval for each dimension of **x** is explored [73]. In Latin Hypercube Sampling the interval of the variables $\mathbf{x} = (x_1 ... x_h)$ are subdivided into bins, where the number of bins corresponds to the number of desired samples. On the interval of each bin a sample is taken from a uniform random distribution. The samples for each of the variables are then combined such that they produce a Latin square, which is where a sample is only represented once in each column and once in each row. An example of a Latin Hypercube Sampling of three variables and with four samples are given in figure 8.4 below:

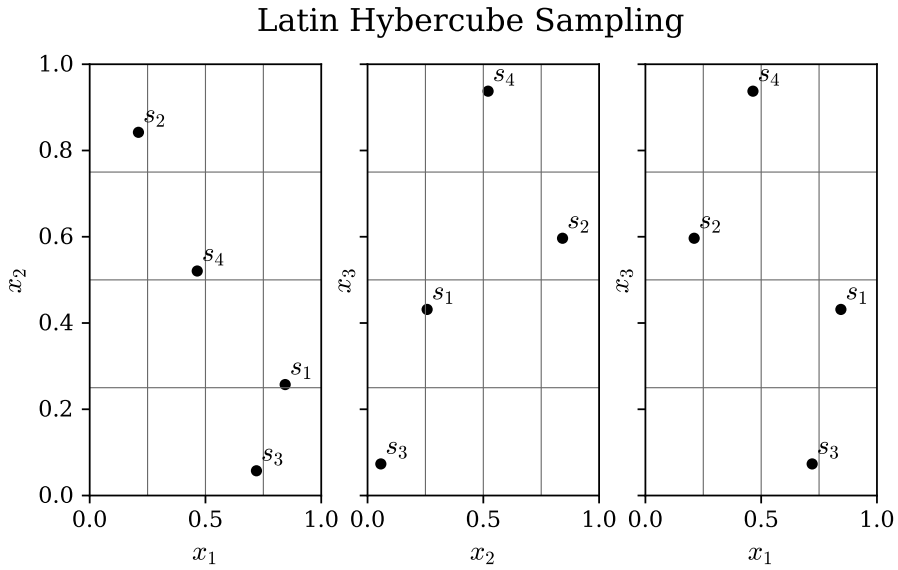

Fig. 8.4: Latin Hypercube Sampling with four samples of 3 variables on the interval $\mathbf{x} \in [0,1]$. Each sub-figure is a projection of the Latin Hypercube down to a Latin square. Each point in the sub-figures is a sample, and is labelled such that the same sample point can be seen in all of the projections.

When all of the sample points have been evaluated they are used to generate a GP and the expected improvement function is maximised. The function is then evaluated at the new $\mathbf{x}$ resulting from the maximisation of the expected improvement function and is added to the sample set. This process is then repeated until the value at the maximum of the expected improvement function is less than a predefined tolerance of the minimum function value in the sample set. This process is shown in figure 8.5, where a one dimensional function is minimised. Initially three samples are taken and the EGO is then applied. The EGO is converged when the maximum value of the expected improvement is less than 0.5% of the minimum function value.

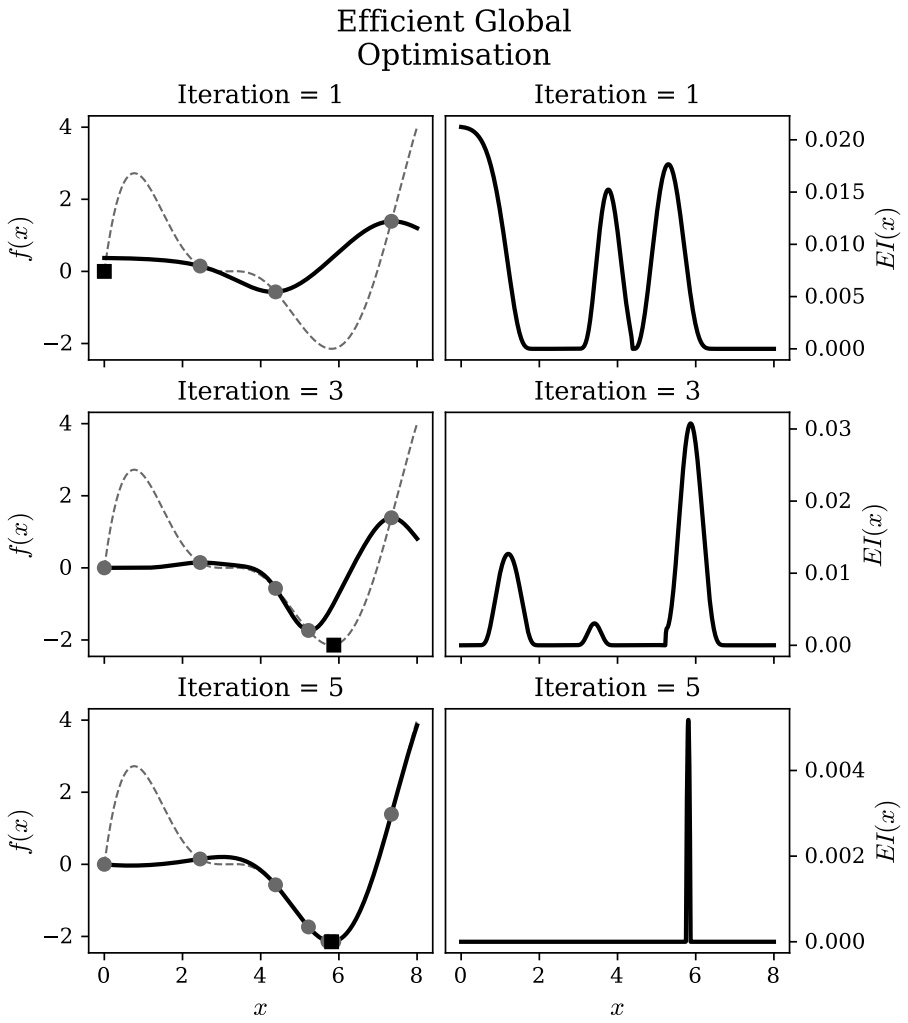

Fig. 8.5: Efficient Global Optimisation process. Three iterations of the process are shown, with the Gaussian Process on the left and the expected improvement on the right. The points in the sample set are represented by a dot, while the new point found by the maximisation of the expected improvement is represented by a square.

Chapter 9

Results

In this chapter the results of the scrubber model will be presented. The results shown are from the model with the heat- and mass transfer coefficients calibrated to the data from a scrubber system aboard an ocean going vessel, as presented in paper D. In addition, results from the model simulating full load on the scrubber with respect to exhaust gas and liquid, will also be presented. Finally, a simulation with an optimised exhaust cover, using the optimisation strategy presented in paper C, will also be presented. The boundary values for the results presented in this chapter corresponds to values of data set 4 presented in paper D [44].

1 Liquid Volume Fraction

In figure 9.1 the liquid volume fraction in the scrubber is shown. It is general for all three cases that there is a larger accumulation of seawater towards the centre of the packed bed. Although for the case with full load, shown in the centre of figure 9.1, the volume fraction is larger compared to the case corresponding to data set 4. This is to be expected as the amount of seawater being injected into the scrubber is 17% higher. Furthermore, it can be seen that the liquid is being pinned under the packed bed towards the outer wall of the scrubber, for the full load case. This is caused by the larger velocity of the exhaust gas and hence drag force, being able to carry the droplets against the force of gravity. As the seawater cannot leave the packed bed in this area, it is forced towards the centre of the scrubber, resulting in a build up of liquid on top of the exhaust cover.

Comparing the case with the optimised exhaust cover, shown rightmost in figure 9.1, to the case corresponding to data set 4, it can be seen that there no discernible difference between the two, except for a slightly thicker layer of liquid on the edge of the exhaust cover.

A thing to note for all cases are the vertical lines of higher liquid volume fraction at the nozzles above the packed bed. The one along the centre line is caused by the symmetry of the mesh, which makes the seawater accumulate. The others are caused be the averaging of the Eulerian-Eulerian framework, which causes the vertical velocity components to cancel out.

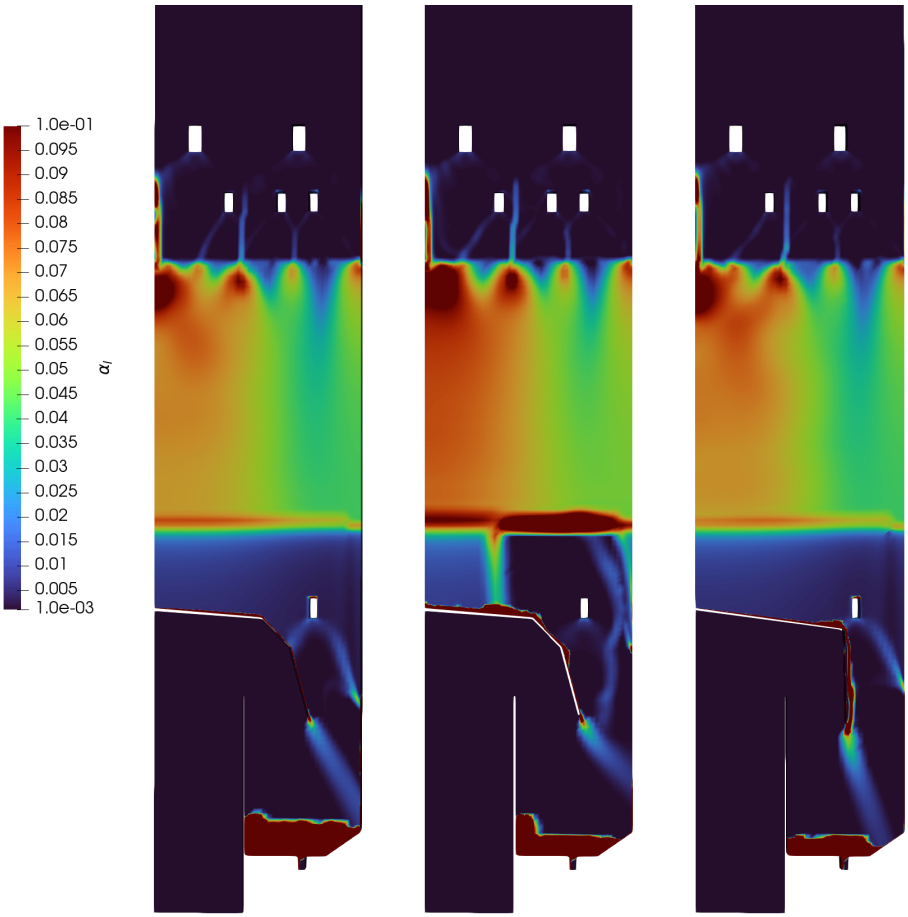

Fig. 9.1: Liquid volume fraction in the scrubber. The scale cuts off at $\alpha_l = 10^{-3}$, to be able to distinguish the differences in the packed bed. This means that the dark blue areas under the packed bed does contain liquid except for the area under the exhaust cover. On the left is the case corresponding to data set 4 in paper D, in the middle is the case for full load on the scrubber, and on the right is the case with the optimised exhaust cover.

2 Exhaust gas velocity

In figure 9.2 tracer streamlines for the exhaust gas are shown. Here it can be seen that the exhaust gas flows towards the outer side of the packed bed for all cases, but to a lesser extent in the full load case. This indicates that the centre of the packed bed is used as efficiently as it could be, had the flow been more uniformly distributed. The reason for this tendency can be attributed to both the exhaust cover and the distribution of liquid in the packed bed. As it can be seen the exhaust cover forces the exhaust gas towards the wall of scrubber where the majority remains until it reaches the packed bed.

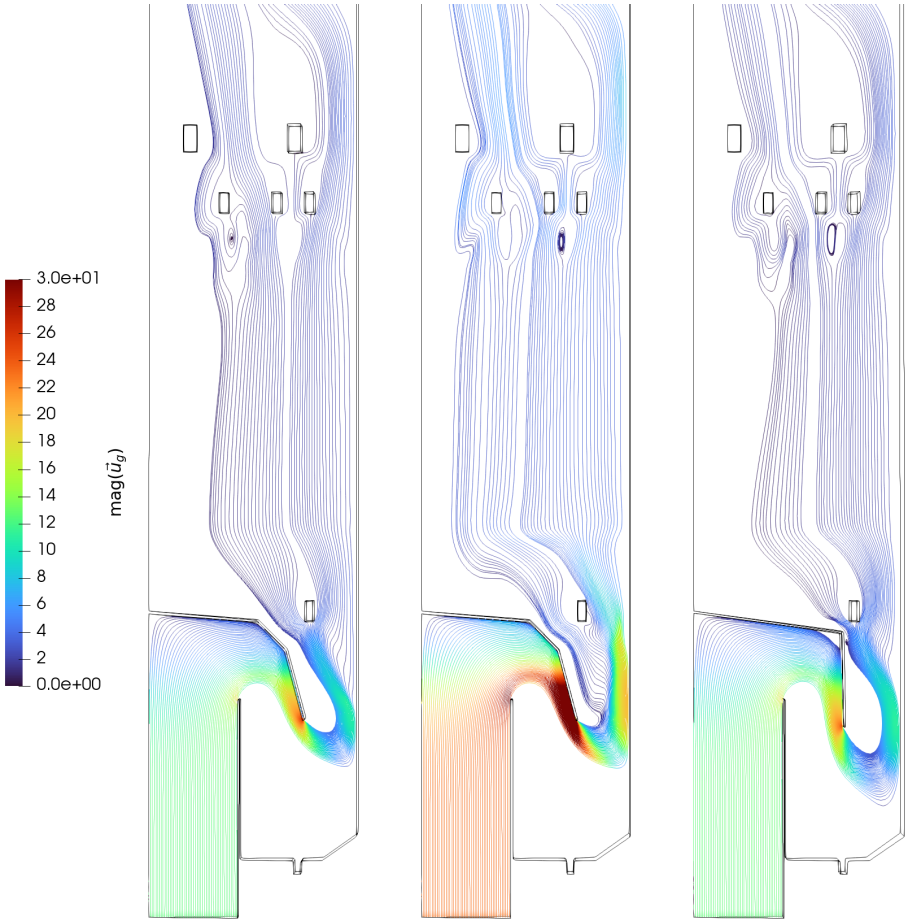

Fig. 9.2: Velocity streamlines for the exhaust gas in the scrubber. On the left is the case corresponding to data set 4 in paper D, in the middle is the case for full load on the scrubber, and on the right is the case with the optimised exhaust cover

Because the liquid volume fraction in the packed bed is higher towards the centre the interfacial forces are higher as well. This results in a larger resistance for the exhaust gas, which then flows through areas with less seawater present as it offers less resistance. As mentioned previously the exhaust gas velocity for the full load case resulted in the seawater being pinned under the packed bed, it can be seen that this is in fact caused by the high velocity of the exhaust gas towards the wall of the scrubber. Comparing to the other two cases where the velocity is lower, it can be seen that the exhaust gas stream is deflected inwards by the seawater coming from the packed bed.

Comparing the flow path resulting from the optimised exhaust cover, as shown in figure 9.2, to the existing design, it can be seen that the abrupt turn that the exhaust gas has to make has been widened, and that the velocity at the lip of the exhaust cover has been reduced. This results in a reduction in the pressure loss of 95 Pa from 799 Pa to 704 Pa.

3 SO_2 concentration

For the case corresponding to data set 4 in paper D, the concentration of SO_2 at the outlet predicted by the model is 33 ppm, whereas for the full load case, the model predicted a concentration of 120 ppm [44]. This is known not to be the case for the real scrubber as it exceeds the emission ratio presented in table 1.1. Here the equivalent for 0.5% sulphur content by mass was shown to be 21.7 $\frac{SO_2}{CO_2}\frac{ppm}{\%v/v}$ and the resulting equivalent predicted by the model is 24.9 $\frac{SO_2}{CO_2}\frac{ppm}{\%v/v}$. Even though data for a full load case is not available, the scrubber is able to reduce the SO_2 concentration to below the 21.7 $\frac{SO_2}{CO_2}\frac{ppm}{\%v/v}$ as this is confirmed during commissioning and testing of the scrubber. This means that the error for the full load case is as least 14.6%. This is however, within the range errors seen in the data set where they ranged from -24% to 25%.

As expected with the exhaust gas flowing towards the outer side of the packed bed it is also in this part of the packed bed that the SO_2 escaping the scrubber is originating from, as shown in figure 9.3. Here it can also be seen that the concentration of SO_2 in the centre of the packed bed is below 10 ppm, for the case corresponding to data set 4 in paper D, due to the excess seawater present in this area. In the full load case it can be seen that more SO_2 is present throughout the packed bed; this, combined with the wider flow path of the exhaust gas through the packed bed is an indication of a better utilisation of the entire bed.

Lastly it can be seen that the case with the optimised exhaust cap has a larger slip of SO_2 from the top of the packed bed. This results in a concentration of SO_2 at the outlet of 47 ppm compared to the 33 ppm for the existing design. This is again caused by the flow path of the exhaust gas, where the

optimised exhaust cover forces more of the exhaust gas to flow along the outer wall of the scrubber.

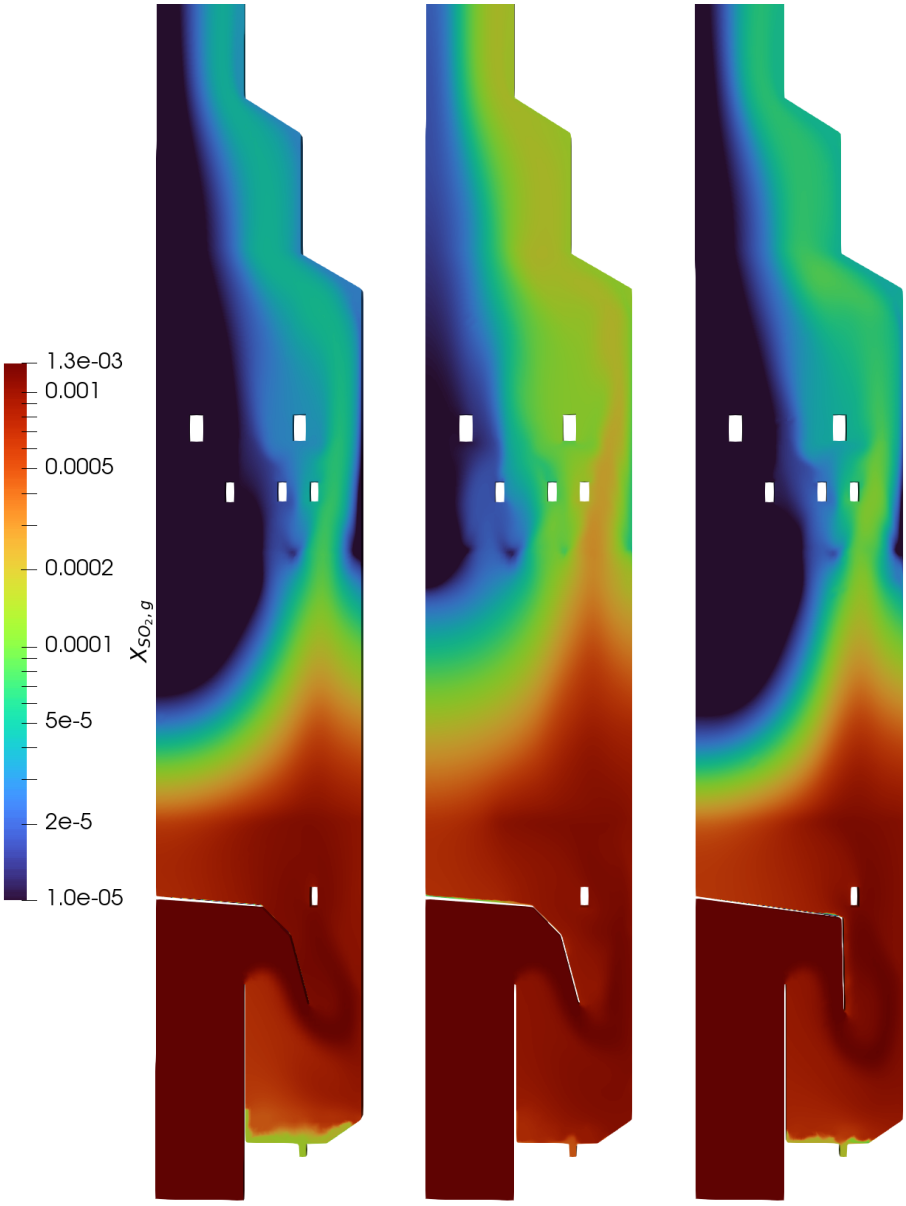

Fig. 9.3: Mole fraction of SO_2 in the exhaust gas in the scrubber. Note that the scale is logarithmic. On the left is the case corresponding to data set 4 in paper D, in the middle is the case for full load on the scrubber, and on the right is the case with the optimised exhaust cover

Chapter 10

Conclusion

A model for a packed bed inline scrubber has been developed using the OpenFOAM library. The model was derived from the existing solver multiphaseEulerFoam, which is based on the Eulerian-Eulerian modelling framework. The model of the packed bed scrubber accounted for phenomena in both the packed bed and in regions where the influence of dispersed droplets is dominant. Furthermore, a chemistry model was implemented which captured the reactions occurring in seawater during the absorption of SO_2.

A model for heat and mass transfer in droplets with internal circulation was developed. The model is based on two sets of streamlines where one relates to a low Reynolds number and the other to a high Reynolds number. Both models were solved numerically over a range of modified Peclet numbers and a correlation between the modified Peclet number and the Nusselt or Sherwood number was developed. The proposed model was validated against temperature measurements of large free falling droplets found in the literature. It was found that for the best fit the low Reynolds number model should be used for Reynolds numbers below 400 and model for high Reynolds numbers should be used above. The results showed that for droplets with a diameter over 3mm the predicted temperature deviated by as much as 40%. However, the temperature differences in the droplets where the largest errors were seen, was around 2-3K, meaning that the absolute error is around 1K.
It was found that existing models for interfacial forces in packed beds was

unable to predict the liquid volume fraction and pressure loss over a packed bed consisting of the IMTP packing material with a large nominal diameter. By combining an existing method for determining the coefficients used in the expressions for gas-solid, liquid-solid, and gas-solid with a definition of wet pressure loss; a method for determining new formulations for the three interfacial forces in a packed bed were developed. This method showed good results both for IMTP-50, which was used in paper B, and IMTP-60 used in the scrubber model. Here, the relative difference in pressure loss between that predicted by the model and the data presented in paper D was within 3%.

The chemistry model implemented in the scrubber model accounted for 5 equilibria reactions, 10 species, and the oxidation of sulphite. The equilibria was solved using expressions for the equilibrium constants found in the literature where some were determined for seawater and others were not. For those not determined for seawater, an activity coefficient was included in the expressions for the equilibrium constants to account for the non-ideal behaviour caused by the ions in seawater. The equilibria were validated against data from the literature and were able to predict the pH of the seawater as more SO_2 was absorbed.

A heat- and mass transfer model for packed beds was derived from existing expressions which was based on empirical correlations and implemented in the scrubber. The expressions for both heat and mass transfer have coefficients which are specific to each type and size of packing material. The coefficients for the gas and liquid side of the phase interface were calibrated for both heat- and mass transfer in a scrubber using the data gathered from an ocean going vessel. The calibration was done using a global derivative free optimisation method call Efficient Global Optimisation which was coupled to the scrubber model. With the calibrated coefficients the error between the model and the data for the SO_2 concentration at the outlet of the scrubber were found to be between -24% and 25%. However, the concentration of SO_2 in the data set are between 23 and 40 ppm, which means that the maximum absolute deviation was within 5 ppm for all but a single data point.

It was found that the largest contributor to the pressure loss in the scrubber was the exhaust cover. Thus, in addition to the scrubber model, a strategy for optimising the exhaust cover in the scrubber was developed and presented in paper C. The optimisation strategy only accounts for the interaction between the exhaust gas and the exhaust cover. This allows for the use of a single phase model, which is significantly cheaper to evaluate computationally. To be able to optimise the design of the exhaust cover the OpenFOAM simulations were coupled to an optimisation algorithm called Method of Feasible

Directions. This allows for the use of constraints on the design of the exhaust cover, which ensures a stable optimisation without invalid geometries and for designs which eliminates the accumulation of water on top of exhaust cover. In the generic scrubber used in paper C, the pressure loss was reduced by 42%. However, in the case where an optimised exhaust cover was implemented in the scrubber model, the reduction in pressure loss was found to be 12%.

References

[1] "A history of flue gas desulfurization systems since 1850," *J. Air Pollut. Control Assoc.*, vol. 27, no. 10, pp. 948–961, Oct. 1977.

[2] IMO, "Historic background," https://www.imo.org/en/OurWork/Environment/Pages/Historic-Background-.aspx, International Maritime Orginisation, Tech. Rep., Dec. 2021, accessed: 2021-12-09.

[3] IMO, "Emission control area," https://www.imo.org/en/OurWork/Environment/Pages/Emission-Control-Areas-(ECAs)-designated-under-regulation-13-of-MARPOL-Annex-VI-(NOx-emission-control).aspx, International Maritime Orginisation, Tech. Rep., Dec. 2021, accessed: 2021-12-09.

[4] P. Elson, E. S. D. Andrade, G. Lucas, R. May, R. Hattersley, E. Campbell, A. Dawson, Stephane Raynaud, Scmc72, B. Little, A. D. Snow, K. Donkers, B. Blay, K. Peter, N. Wilson, P. Peglar, Lbdreyer, Andrew, J. Szymaniak, A. Berchet, C. Bosley, L. Davis, Filipe, J. Krasting, M. Bradbury, D. Kirkham, Stephenworsley, Clément, G. Caria, and M. Hedley, "Scitools/cartopy: v0.20.1," Exeter, Devon, 2021. [Online]. Available: https://scitools.org.uk/cartopy

[5] MEPC, "Resolution mepc.176(58)," Oct. 2008.

[6] MEPC, "Resolution mepc.259(68)," May 2015. [Online]. Available: https://www.imo.org/en/KnowledgeCentre/IndexofIMOResolutions/Pages/MEPC-2014-15.aspx

[7] A. Andreasen and S. Mayer, "Use of seawater scrubbing for so2 removal from marine engine exhaust gas," *Energy and Fuels*, vol. 21, no. 6, pp. 3274–3279, Nov. 2007.

[8] M. Production, "Sox scrubber modes," Jun. 2022, https://meproduction.com/front-page/marine-exhaust-gas-scrubbers/.

[9] L. Osipova, E. Georgeff, and B. Comer, "Global scrubberwashwater dischargesunder imo's 2020 fuel sulfur limit," icct, Tech. Rep., 2021.

[10] A. Gómez, N. Fueyo, and A. Tomás, "Detailed modelling of a flue-gas desulfurisation plant," *Computers and Chemical Engineering*, vol. 31, no. 11, pp. 1419–1431, nov 2007.

[11] L. Marocco and F. Inzoli, "Multiphase euler–lagrange cfd simulation applied to wet flue gas desulphurisation technology," *International Journal of Multiphase Flow*, vol. 35, no. 2, pp. 185–194, 2009. [Online]. Available: https://www.sciencedirect.com/science/article/pii/S0301932208001341

[12] J. Qu, N. Qi, K. Zhang, L. Li, and P. Wang, "Wet flue gas desulfurization performance of 330 mw coal fired power unit based on computational fluid dynamics region identification of flow pattern and transfer process," *Chinese Journal of Chemical Engineering*, vol. 29, pp. 13–26, jan 2021.

[13] A. H. Abdulsattar, S. Sridhar, and L. A. Bromley, "Thermodynamics of the sulfur dioxide-seawater system," *AIChE Journal*, vol. 23, no. 1, pp. 62–68, Jan. 1977.

[14] M. I. Lamas, C. G. Rodríguez, J. D. Rodríguez, and J. Telmo, "Numerical model of so2 scrubbing with seawater applied to marine engines," *Polish Maritime Research*, vol. 23, no. 2, pp. 42–47, 2016.

[15] A. Simonsen, "Modelling and analysis of seawater scrubbers for reducing sox emissions from marine engines," Ph.D. dissertation, 2018, phD supervisors: Associate Professor Kim Sørensen, Aalborg University Søren Mølgaard, Alfa Laval Aalborg Assistant PhD supervisors: Associate Professor Thomas J. Condra, Aalborg University Professor Lasse A. Rosendahl, Aalborg University Ruddi K. Mortensen, Alfa Laval Aalborg.

[16] D. Liu, Z. Xiong, J. Jin, T. Wall, and R. Stanger, "Conceptual design of a packed bed for the removal of SO 2 in oxy-fuel combustion prior to compression," *International Journal of Greenhouse Gas Control*, vol. 53, pp. 65–78, oct 2016.

[17] J. Zhou, S. Zhou, and Y. Zhu, "Experiment and prediction studies of marine exhaust gas so2 and particle removal based on NaOH solution with a u-type scrubber," *Industrial and Engineering Chemistry Research*, vol. 56, no. 43, pp. 12 376–12 384, oct 2017.

[18] I. Iliuta and M. C. Iliuta, "Modeling of so2 seawater scrubbing in countercurrent packed-bed columns with high performance packings," *Separation and Purification Technology*, vol. 226, pp. 162–180, nov 2019.

[19] I. Iliuta and F. Larachi, "Modeling and simulations of NOx and SO2 seawater scrubbing in packed-bed columns for marine applications," *Catalysts*, vol. 9, no. 6, p. 489, may 2019.

[20] T. O. Foundation, *OpenFOAM C++ Source Code Guide*, 2021. [Online]. Available: https://cpp.openfoam.org/v9/

[21] G. Al-Enezi, Ettouney, H. El-Dessouky, and N. Fawzi, "Solubility of sulfur dioxide in seawater," *Industrial and Engineering Chemistry Research*, vol. 40, no. 5, pp. 1434–1441, feb 2001.

[22] A. G. Dickson and C. Goyet, "Handbook of methods for the analysis of the various parameters of the carbon dioxide system in sea water. version 2," Tech. Rep., Sep. 1994. [Online]. Available: https://www.osti.gov/biblio/10107773

[23] A. G. Dickson, "The development of the alkalinity concept in marine chemistry," *Marine Chemistry*, vol. 40, no. 1, pp. 49–63, 1992, progress in Marine Chemistry. [Online]. Available: https://www.sciencedirect.com/science/article/pii/030442039290047E

[24] A. G. Dickson, "An exact definition of total alkalinity and a procedure for the estimation of alkalinity and total inorganic carbon from titration data," *Deep Sea Research Part A. Oceanographic Research Papers*, vol. 28, no. 6, pp. 609–623, 1981. [Online]. Available: https://www.sciencedirect.com/science/article/pii/0198014981901217

[25] D. A. Wolf-Gladrow, R. E. Zeebe, C. Klaas, A. Körtzinger, and A. G. Dickson, "Total alkalinity: The explicit conservative expression and its application to biogeochemical processes," *Marine Chemistry*, vol. 106, no. 1, pp. 287–300, 2007, special issue: Dedicated to the memory of Professor Roland

Wollast. [Online]. Available: https://www.sciencedirect.com/science/article/pii/S0304420307000047

[26] P. Atkins and J. de Paula, *ATKINS' PHYSICAL CHEMISTRY*, 8th ed. W. H. Freeman and Company 41 Madison Avenue New York, NY 10010: W. H. Freeman and Company, 2006.

[27] C. W. Davies, *Ion Association*. Butterworths, 1962.

[28] J. Hamelin, J. B. Mehl, and M. R. Moldover, "The static dielectric constant of liquid water between 274 and 418 k near the saturated vapor pressure," *International Journal of Thermophysics*, vol. 19, no. 5, pp. 1359–1380, 1998.

[29] F. J. Millero, "The physical chemistry of seawater," *Annual Review of Earth and Planetary Sciences*, vol. 2, no. 1, pp. 101–150, May 1974.

[30] A. G. Dickson, "Standard potential of the reaction: Agcl(s) + 12h2(g) = ag(s) + hcl(aq) and and the standard acidity constant of the ion hso4- in synthetic sea water from 273.15 to 318.15 k," *The Journal of Chemical Thermodynamics*, vol. 22, no. 2, pp. 113–127, 1990. [Online]. Available: https://www.sciencedirect.com/science/article/pii/002196149090074Z

[31] F. J. Millero, T. B. Graham, F. Huang, H. Bustos-Serrano, and D. Pierrot, "Dissociation constants of carbonic acid in seawater as a function of salinity and temperature," *Marine Chemistry*, vol. 100, no. 1, pp. 80–94, 2006. [Online]. Available: https://www.sciencedirect.com/science/article/pii/S0304420305001921

[32] J. A. Michalski, "Sulphur dioxide solubility in aqueous solutions of calcium or magnesium sulphites," *Chemical Engineering and Technology*, vol. 23, no. 6, pp. 521–525, 2000. [Online]. Available: https://onlinelibrary.wiley.com/doi/abs/10.1002/1521-4125%28200006%2923%3A6%3C521%3A%3AAID-CEAT521%3E3.0.CO%3B2-G

[33] J.-Z. Zhang and F. J. Millero, "The rate of sulfite oxidation in seawater," *Geochimica et Cosmochimica Acta*, vol. 55, no. 3, pp. 677–685, 1991. [Online]. Available: https://www.sciencedirect.com/science/article/pii/001670379190333Z

[34] R. Sander, "Compilation of henry's law constants (version 4.0) for water as solvent," *Atmospheric Chemistry and Physics*, vol. 15, no. 8, pp. 4399–4981, Apr. 2015.

[35] S. Kumar and D. Ramkrishna, "On the solution of population balance equations by discretization—i. a fixed pivot technique," *Chemical Engineering Science*, vol. 51, no. 8, pp. 1311–1332, apr 1996.

[36] H. S. Aly, Y. A. Eldrainy, K. M. Saqr, T. M. Lazim, and M. N. M. Jaafar, "A mathematical model for predicting spray atomization characteristics in an eulerian–eulerian framework," *Int Commun Heat Mass*, vol. 37, no. 6, pp. 618–623, Jul. 2010.

[37] N. I. Kolev, *Multiphase Flow Dynamics 2 Thermal and Mechanical Interactions*. Springer London, Limited, 2007.

[38] F. Menter, M. Kuntz, and R. Langtry, "Ten years of industrial experience with the sst turbulence model," *Heat and Mass Transfer*, vol. 4, 01 2003.

[39] M. Pilch, "Acceleration induced fragmentation of liquid drops," Ph.D. dissertation, University of Virginia, 1981.

[40] Y. Liao and D. Lucas, "A literature review of theoretical models for drop and bubble breakup in turbulent dispersions," *Chemical Engineering Science*, vol. 64, no. 15, pp. 3389–3406, aug 2009.

[41] C. Coulaloglou and L. Tavlarides, "Description of interaction processes in agitated liquid-liquid dispersions," *Chemical Engineering Science*, vol. 32, no. 11, pp. 1289–1297, 1977.

[42] M. Hsia and L. L. Tavlarides, "Simulation analysis of drop breakage, coalescence and micromixing in liquid-liquid stirred tanks," *The Chemical Engineering Journal*, vol. 26, no. 3, pp. 189–199, jan 1983.

[43] C. Lee, L. Erickson, and L. Glasgow, "DYNAMICS OF BUBBLE SIZE DISTRIBUTION IN TURBULENT GAS-LIQUID DISPERSIONS," *Chemical Engineering Communications*, vol. 61, no. 1-6, pp. 181–195, nov 1987.

[44] M. Poulsen, H. Ström, S. Sasic, K. Sørensen, and T. Condra, "Development and calibration of a model for packed bed marine scrubbers aboard ocean-going vessels," Jun. 2022, under review.

[45] M. Poulsen, K. Sørensen, and T. Condra, "Comparison of two-phase porosity models for high capacity random packing," *E3S Web Conf.*, vol. 321, p. 01015, 2021. [Online]. Available: https://doi.org/10.1051/e3sconf/202132101015

[46] H. J. Holterman, *Kinetics and evaporation of water drops in air*. CIP-DATA ROYAL LIBRARY, DEN HAAG, NL, 2003.

[47] A. Attou, C. Boyer, and G. Ferschneider, "Modelling of the hydrodynamics of the cocurrent gas–liquid trickle flow through a trickle-bed reactor," *Chemical Engineering Science*, vol. 54, no. 6, pp. 785–802, 1999.

[48] M. Fourati, V. Roig, and L. Raynal, "Liquid dispersion in packed columns: Experiments and numerical modeling," *Chemical Engineering Science*, vol. 100, pp. 266–278, 2013, 11th International Conference on Gas-Liquid and Gas-Liquid-Solid Reactor Engineering.

[49] K. Lappalainen, V. Alopaeus, M. Manninen, and J. Aittamaa, "Improved hydrodynamic model for wetting efficiency, pressure drop, and liquid holdup in trickle-bed reactors," *Industrial & Engineering Chemistry Research*, vol. 47, no. 21, pp. 8436–8444, 2008.

[50] J. R. Finn and J. E. Galvin, "Calibration of drag models for mesoscale simulation of gas–liquid flow through packed beds," *Chemical Engineering Science*, vol. 172, pp. 722–730, 2017.

[51] Sulzer, "Sulcol 3.3.4," 2021. [Online]. Available: https://www.sulzer.com/en/shared/products/sulcol-for-windows

[52] K. Lappalainen, M. Manninen, and V. Alopaeus, "CFD modeling of radial spreading of flow in trickle-bed reactors due to mechanical and capillary dispersion," *Chem Eng Sci*, vol. 64, no. 2, pp. 207–218, Jan. 2009.

[53] D. Dzhonova-Atanasova, N. Kolev, and S. Nakov, "Determination of liquid radial spreading coefficients of some highly effective packings," *Chemical Engineering & Technology*, vol. 30, no. 2, pp. 202–207, 2007. [Online]. Available: https://onlinelibrary.wiley.com/doi/abs/10.1002/ceat.200600327

[54] Z. Cihla and O. Schmidt, "A study of the flow of liquid when freely trickling over the packing in a cylindrical tower," *Collect. Czech. Chem. Commun.*, vol. 22, no. 3, pp. 896–907, 1957.

[55] M. Poulsen, K. Sørensen, and T. Condra, "Heat and mass transfer model for droplets with internal circulation," *Linköping Electronic Conference Proceedings*, vol. 176, no. 27, pp. 195–202, mar 2021.

[56] R. B. Bird, W. E. Stewart, and E. N. Lightfoot, *Transport phenomena*, 2nd ed. New York: J. Wiley, 2002.

[57] G. Ahmed and M.Yovanovich, "Approximate analytical solution of forced convection heat transfer from isothermal spheres for all prandtl numbers," *Journal of Heat Transfer-transactions of The Asme - J HEAT TRANSFER*, 1994.

[58] N. Froessling, "Uber die verdunstung fallender tropfen," *Gerlands Beitrage zur Geophysik*, vol. 52, pp. 107–216, 1938.

[59] J. Hadamard, "Mouvement permanent lent d'une sphere liquide et visqueuse dans un liquide visqueux," *C. R. Acad. Sci.*, vol. 152, pp. 1735–1752, 1911.

[60] D. R. Olander, "The handlos-baron drop extraction model," *AIChE Journal*, vol. 12, no. 5, pp. 1018–1019, 1966.

[61] R. Billet and M. Schultes, "Prediction of mass transfer columns with dumped and arranged packings," *Chemical Engineering Research and Design*, vol. 77, no. 6, pp. 498–504, Sep. 1999.

[62] R. Higbie, "The rate of absorption of a pure gas into a still liquid during short period of exposure," *Trans. Am. Inst. Chem. Eng.*, vol. 31, 01 1935.

[63] Y. Cengel, *Fundamentals of thermal-fluid sciences*. New York, NY: McGraw-Hill Education, 2017.

[64] R. Billet, *Packed Towers*. Wiley, feb 1995.

[65] ANSYS, *ANSYS Fluent User's Guide*, Southpointe 275 Technology DriveCanonsburg, PA 15317, Nov. 2013.

[66] D. B. Spalding, "A single formula for the "law of the wall"," *Journal of Applied Mechanics*, vol. 28, no. 3, pp. 455–458, sep 1961.

[67] ANSYS, *ANSYS Fluent Theory Guide*, Southpointe 275 Technology DriveCanonsburg, PA 15317, Nov. 2013.

[68] P. Wu, L. Tseng, and G. Faeth, "Primary breakup in gas/liquid mixing layers for turbulent liquids," jan 1992.

[69] A. Bailey, W. Balachandran, and T. Williams, "The rosin—rammler size distribution for liquid droplet ensembles," *Journal of Aerosol Science*, vol. 14, no. 1, pp. 39–46, jan 1983.

[70] D. R. Jones, M. Schonlau, and W. J. Welch, "Efficient global optimization of expensive black-box functions," *Journal of Global Optimization*, vol. 13, no. 4, pp. 455–492, 1998.

[71] B. Adams, L. Bauman, W. Bohnhoff, K. Dalbey, M. Ebeida, J. Eddy, M. Eldred, P. Hough, K. Hu, J. Jakeman, J. Stephens, L. Swiler, D. Vigil, and T. Wildey, "Dakota, a multilevel parallel object-oriented framework for design optimization, parameter estimation, uncertainty quantification, and sensitivity analysis: Version 6.0 user's manual," techreport 6.15, July 2021.

[72] J. M. Gablonsky, "Direct vesion 2.0, user guide," Tech. Rep., 2001.

[73] J. Lawson, *Design and analysis of experiments with R*. Boca Raton: CRC Press, Taylor & Francis Group, 2015.

[74] K. G. Nayar, M. H. Sharqawy, L. D. Banchik, and J. H. L. V, "Thermophysical properties of seawater: A review and new correlations that include pressure dependence," *Desalination*, vol. 390, pp. 1–24, jul 2016.

[75] M. H. Sharqawy, J. H. Lienhard, and S. M. Zubair, "Thermophysical properties of seawater: a review of existing correlations and data," *Desalination and Water Treatment*, vol. 16, no. 1-3, pp. 354–380, apr 2010.

[76] B. McBride, S. Gordon, and M. A. Reno, "Coefficients for calculating thermodynamic and transport properties of individual species," in *NASA Technical Memorandum 4513*, 1993.

[77] W. Sutherland, "LII. the viscosity of gases and molecular force," *The London, Edinburgh, and Dublin Philosophical Magazine and Journal of Science*, vol. 36, no. 223, pp. 507–531, dec 1893.

[78] A. Einstein, "Über die von der molekularkinetischen theorie der wärme geforderte bewegung von in ruhenden flüssigkeiten suspendierten teilchen," *Annalen der Physik*, vol. 322, no. 8, pp. 549–560, 1905.

[79] R. Perry, *Perry's chemical engineers' handbook*. New York: McGraw-Hill, 2008.

[80] Y. Cengel, *Heat and mass transfer : fundamentals and applications*. New York, NY: McGraw Hill Education, 2015.

[81] A. Koliadima, J. Kapolos, and L. Farmakis, "Diffusion coefficients of so2 in water and partition coefficients of so2 in water–air interface at different temperature and pH values," *Instrumentation Science and Technology*, vol. 37, no. 3, pp. 274–283, Apr. 2009.

[82] S. Andrew, "A simple method of measuring gaseous diffusion coefficients," *Chemical Engineering Science*, vol. 4, no. 6, pp. 269–272, Dec. 1955.

[83] A. E. Rabe and J. F. Harris, "Vapor liquid equilibrium data for the binary system sulfur dioxide and water." *Journal of Chemical and Engineering Data*, vol. 8, no. 3, pp. 333–336, Jul. 1963.

[84] F. J. Millero, J. P. Hershey, G. Johnson, and J.-Z. Zhang, "The solubility of SO2 and the dissociation of h2so3 in NaCl solutions," *Journal of Atmospheric Chemistry*, vol. 8, no. 4, pp. 377–389, May 1989.

Appendices

I Physical properties

In OpenFOAM's thermo-physical libraries there are many predefined functions for determining the physical properties of a fluid. In the model a mixture of the pre-defined and user-defined functions are utilised to model the properties of the gas and liquid phase. Both phases in the model are multi-component phases and OpenFOAM uses mass based averaging of the coeffients for each species to determine the given property of the phase:

$$\phi = f(\bar{x}) \tag{I.1}$$

$$\bar{x} = \sum_{i}^{n} y_i x_i \tag{I.2}$$

where ϕ is the property of interest and y_i is the mass fraction of species i out of n and x is the coefficients for the given expression $f(x)$.

I.1 Density

Liquid phase Considering that the liquid phase consists of water, salt and a minute amount of absorbed species from the gas phase, the density of the liquid phase is modelled as pure water with the remaining components lumped into a solute group. The density for two constituents in the liquid phase are given as an inverse polynomial which is given as:

$$\rho_i = \frac{1}{a_0 + a_1 T + a_2 T^2 - a_3 p - a_4 p T} \tag{I.3}$$

where ρ_i is the density of the species i, a_j is the species specific coefficicents, p is the pressure and T is the temperature of the phase.

As an expression for the density of seawater in this form is not readily available in the literature, the coefficients for equation I.3 are fitted using an

existing correlation for seawater [74, 75]. The correlation used for fitting the coefficients are given as [74]:

$$\begin{aligned}\rho_{sw}(T,S) =& a_1 + a_2 T_C + a_3 T_C^2 + a_4 T_C^3 + a_5 T_C^4 + \\ & b_1 S + b_2 S T_C + b_3 S T_C^2 + b_4 S T_C^3 + b_5 S^2 T_C^2\end{aligned} \tag{I.4}$$

$$\begin{aligned}a_1 =& 9.999 \times 10^2 & a_2 &= 2.034 \times 10^{-2} & a_3 &= -6.162 \times 10^{-3} \\ a_4 =& 2.261 \times 10^{-5} & a_5 &= -4.657 \times 10^{-8} & & \\ b_1 =& 8.020 \times 10^2 & b_2 &= -2.001 \times 10^0 & b_3 &= 1.677 \times 10^{-2} \\ b_4 =& -3.060 \times 10^{-5} & b_5 &= -1.613 \times 10^{-5} & &\end{aligned}$$

where S is the salinity in kg/kg and T_C is the temperature of the phase in °C.

To fit the coefficients in equation I.3 the density provided by equation I.4 is divided according to equation I.2 such that:

$$\rho_{sw} = \rho_{H_2O} y_{H_2O} + \rho_{sol} y_{sol} \tag{I.5}$$

As the liquid can be considered as incompressible the pressure terms in equation I.3 are neglected when fitting the coefficients. The coefficients found for pure water and the solutes are presented in table I.1.

specie	a_0 $\times 10^{-3}$	a_1 $\times 10^{-3}$	a_2 $\times 10^{-9}$	a_3	a_4
H_2O	1.279	−2.093	3.916	0.000	0.000
Solutes	−1.197	8.778	−12.98	0.000	0.000

Table I.1: Coefficient for modelling the the density of water and the solutes using equation I.3

In figure I.1 a comparison between the expressions for the density of seawater is shown. It can be seen that there is good agreement between the two with a mean error of 0.27‰and a maximum 0.68‰

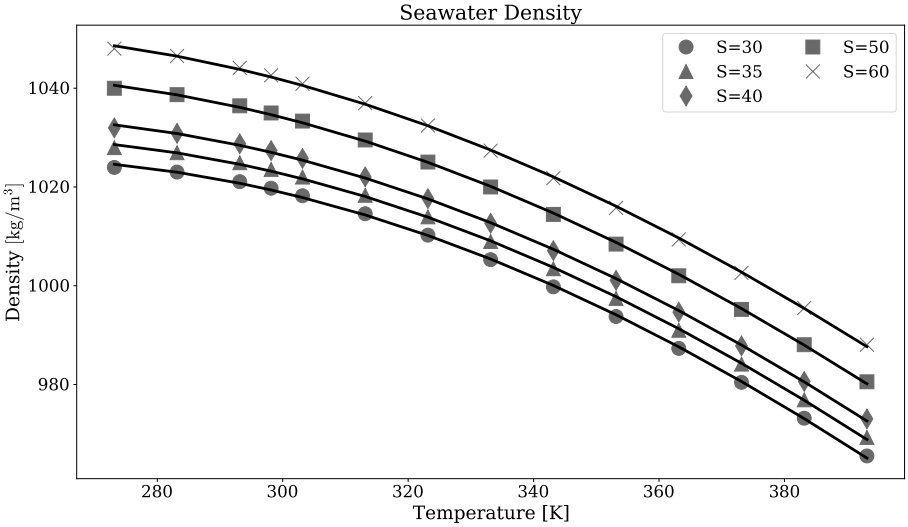

Fig. I.1: Density of seawater at varying temperature and salinities. The markers are derived from equation I.4 and the lines are derived from equiation I.5, with the coefficients from table I.1.

Gas phase Assuming that the gas phase is ideal, the density of the species is simply given by the ideal gas law:

$$\rho_i = \frac{p}{R_i T} \tag{I.6}$$

where ρ_i is the density of the species, p is the pressure, R_i is the species specific gas constant and T is the temperature of the gas phase.

I.2 Heat Capacity

Liquid phase For the liquid phase a polynomial expression is used for determining the specific heat and enthalpy. The expression for these are given below:

$$C_p(T) = \sum_{i=0}^{7} a_i T^i \tag{I.7}$$

$$H^o(T) = \sum_{i=0}^{7} \frac{a_i T^{i+1}}{i+1} + b_1 \tag{I.8}$$

where T is the temperature, a_i is the polynomial coefficients, and b_1 is the integration constant, which is used to adjust the enthalpy to standard conditions.

The value for the heat capacity of seawater is given as [75]:

$$C_p = \left(A + BT + CT^2 + DT^3\right) \times 10^3 \tag{I.9}$$
$$A = 5.328 \times 10^3 - 9.76 \times 10^1 S + 4.04 \times 10^{-1} S^2$$
$$B = -6.913 + 7.351 \times 10^{-1} S - 3.15 \times 10^{-3} S^2$$
$$C = 9.6 \times 10^{-3} - 1.927 \times 10^{-3} S + 8.23 \times 10^{-6} S^2$$
$$D = 2.5 \times 10^{-6} + 1.666 \times 10^{-6} S - 7.125 \times 10^{-9} S^2$$

The specific heat of seawater does not simply scale with the mass fraction of pure water. When the salinity increases the heat capacity of seawater will be lower than that of the corresponding mass fraction of pure water. Therefore the specific heat of the solutes is modelled as being negative. Despite the seeming absurdity of this it does not affect any of the other properties in the liquid species. The coefficients for pure water and solutes used to model the heat capacity and enthalpy for seawater are presented in table I.2:

species	a_0 $\times 10^{-3}$	a_1 $\times 10^{-2}$	a_2 $\times 10^{-1}$	a_3 $\times 10^{-2}$
H_2O	6475	-23.57	9.747	-1.033
Solutes	-1.250	-2.918	-60.51	7.722

species	a_4 $\times 10^{-5}$	a_5 $\times 10^{-7}$	a_6 $\times 10^{-10}$	a_7 $\times 10^{-14}$	b_1 $\times 10^{7}$
H_2O	4.865	-1.212	1.566	-8.298	-1.587
Solutes	-39.92	10.46	-13.91	75.06	-1.587

Table I.2: Polynomial coefficient for the specific heat and absolute enthalpy of seawater as given by equations I.7 and I.8

In figure I.2 a comparison between the heat capacity for seawater and polynomial expression is shown. It can be seen that there is good agreement at lower salinities, but at salinities above 50 $\frac{\text{g}}{\text{kg}}$ the polynomial expression starts to deviate. However, the maximum error at a salinity of 60 $\frac{\text{g}}{\text{kg}}$ is 0.8% which should be insignificant.

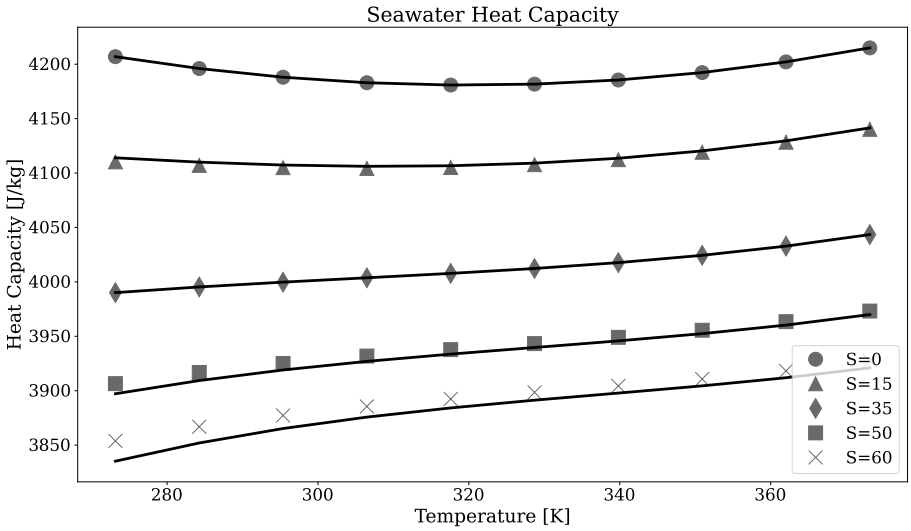

Fig. I.2: Heat capacity of seawater at varying temperature and salinities. The markers are derived from equation I.9 and the lines are derived from equiation I.5, with the coefficients from table I.2.

Gas phase To model the heat capacity and enthalpy of the gas phase a JANAF polynomial is used for each species in the gas phase. The heat capacity and absolute enthalpy can be given as [76]:

$$\frac{C_p(T)}{R} = a_0 + a_1 T + a_2 T^2 + a_3 T^3 + a_4 T^4 \tag{I.10}$$

$$\frac{H^o(T)}{R} = a_0 T + a_1 \frac{T^2}{2} + a_2 \frac{T^3}{3} + a_3 \frac{T^4}{4} + a_4 \frac{T^5}{5} + b_1 \tag{I.11}$$

where C_p is the heat capacity, H^o is the absolute enthalpy, R is the universal gas constant, and T is the temperature of the gas phase.

The JANAF coefficients for the individual species in gas phase are given in Table I.3

species	a_0 $\times 10^0$	a_1 $\times 10^{-3}$	a_2 $\times 10^{-6}$	a_3 $\times 10^{-9}$	a_4 $\times 10^{-12}$	b_1 $\times 10^3$	T_{low}
O_2	3.782	-2.997	9.847	-9.681	3.244	-1.064	200
N_2	3.531	-0.1237	-0.5030	2.435	-1.409	-1.047	200
CO_2	2.357	8.985	-7.124	2.469	-0.1437	-48.37	200
SO_2	3.267	5.324	0.6844	-5.281	2.559	-36.91	300
H_2O	4.199	-2.036	6.520	-5.488	1.772	-3.029	200

Table I.3: JANAF coefficients for the species in the gas phase [76]. The coefficients are all valid up to a temperature of 1000K.

It should be noted that validity of the JANAF polynomial for SO_2 is only valid down to a temperature of 300K (27°C) which is above the temperature of the seawater. However, as the fraction of SO_2 in the gas is relatively small, any errors that are be introduced by extrapolating the values for C_p and H^o are neglected.

I.3 Transport properties

In OpenFOAM's thermo-physical library the viscosity and thermal conductivity are defined by a single transport model. Therefore the two transport properties has to be considered simultaneously.

Liquid phase For the liquid phase a temperature dependent polynomial expression is used to model the transport properties. The polynomial can be expressed as:

$$\phi = \sum_{i=0}^{4} a_i T^i \tag{I.12}$$

where a_i is the coefficient for the i$^{\text{th}}$ term in the polynomial and T is the temperature.

For both the viscosity and thermal conductivity the dependence on salinity is minimal. Therefore, all species in the liquid phase are assigned the same polynomial as for standard seawater with a salinity of 35 g/kg. The expression for the viscosity of seawater is given as [75]:

$$\mu = \exp\left(-10.7019 + \frac{604.129}{139.18 + T_c}\right)(1 + AS + BS^2) \tag{I.13}$$
$$A = 1.474 \times 10^{-3} + 1.5 \times 10^{-5} T_c - 3.927 \times 10^{-8} T_c^2$$
$$B = 1.073 \times 10^{-5} - 8.5 \times 10^{-8} T_c + 2.230 \times 10^{-10} T_c^2$$

where T_c is the temperature in °C and S is the salinity in g/kg.

For the thermal conductivity the expression given in equation I.14 is used. The expression has been modified to return the result in $\mathrm{W/(m\,K)}$ as the original unit is in $\mathrm{mW/(m\,K)}$ [75]:

$$\begin{aligned} \kappa &= 10^{A+B-3} \\ A &= \log(240 + 0.0002S) \\ B &= 0.434\left(2.3 - \frac{343.5 + 0.037S}{T}\right)\left(1 - \frac{T}{647 + 0.03S}\right)^{1/3} \end{aligned} \tag{I.14}$$

where T_c is the temperature and S is the salinity in g/kg.

Fitting the expressions in equations I.13 and I.14 to the polynomial in equation I.12 results in the coefficients presented in table I.4:

	a_0 $\times 10^{-1}$	a_1 $\times 10^{-3}$	a_2 $\times 10^{-5}$	a_3 $\times 10^{-9}$	a_4 $\times 10^{-13}$
μ	3.64240691	-4.16666547	1.79857614	-34.6390612	250.798753
κ	-6.21726945	7.47604442	-1.32931248	7.01734298	-3.71396985

Table I.4: Coefficient used in equation I.16 to estimate viscosity and thermal conductivity [76].

A comparison of the polynomial expressions and the expressions to which they are fitted are shown in figure I.3:

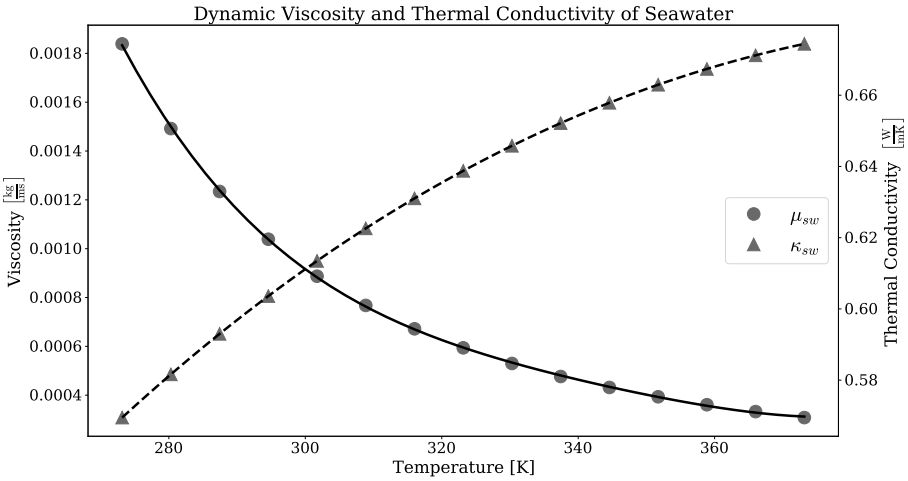

Fig. I.3: Viscosity and thermal conductivity of seawater with a salinity of 35 g/kg. The markers are derived from equations I.13 and I.14 for the viscosity and thermal conductivity, respectively. While the lines are derived from the polynomial expression in equation I.12 with the coefficients from table I.4.

Gas phase For the gas phase the viscosity and thermal conductivity of each species is modeled by means of the Sutherland equation which can be given as [77]:

$$\phi = A_\phi \frac{T^{2/3}}{T + T_\phi} \tag{I.15}$$

Where ϕ is either the viscosity or thermal conductivity, T is the temperature of the gas phase, and A_ϕ and T_ϕ are species specific constants.

The species specific constants in equation I.15 are not readily available in literature for all the species in the gas phase. Therefore the constants A_ϕ and T_ϕ are determined by fitting the Sutherland equation to another expression where the coefficients for all the species are known [76]:

$$\phi = \exp\left(A_{J,\phi} \ln(T) + \frac{B_{J,\phi}}{T} + \frac{C_{J,\phi}}{T^2} + D_{J,\phi}\right) \tag{I.16}$$

It should be noted that the units in equation I.16 is µP for the viscosity and $\mu W/(cm\,K)$ for the thermal conductivity. Therefore, the result of equation I.16 has to be scaled with a factor of 10^{-7} for the viscosity and 10^{-4} for the thermal conductivity to have them expressed in base SI-units. The coefficients for each of the species in the gas phase are given in table I.5:

ϕ	specie	$A_{J,\phi}$ $\times 10^0$	$B_{J,\phi}$ $\times 10^2$	$C_{J,\phi}$ $\times 10^4$	$D_{J,\phi}$ $\times 10^0$
μ	O_2	0.61936357	-0.44608607	-0.13460714	1.9597562
μ	N_2	0.60443938	-0.43632704	-0.088441949	1.8972150
μ	CO_2	0.54330318	-1.8823898	0.88726567	2.4499362
μ	SO_2	0.52954513	-2.6860106	1.7696352	2.5434068
μ	H_2O	0.78387780	-3.8260408	4.9040158	0.85222785
κ	O_2	0.81595343	-0.343668562	0.22785080	1.0050999
κ	N_2	0.94306384	1.2279898	-1.1839435	-0.10668773
κ	CO_2	0.53726173	-4.9928331	3.7397504	3.2903619
κ	SO_2	0.53161859	-4.6428334	3.4368389	2.8729848
κ	H_2O	1.55414431	0.66106305	0.55969886	-3.9259598

Table I.5: Coefficient used in equation I.16 to estimate viscosity and thermal conductivity [76].

The coefficients in table I.5 are valid it from 300K 1000K which is in the high range, and is well beyond the range required for modelling the gas phase. Therefore the coefficients for the Sutherland equation are fitted in the temperature span 300K - 623.15K. A comparison of the fitted transport properties is shown in figure I.4:

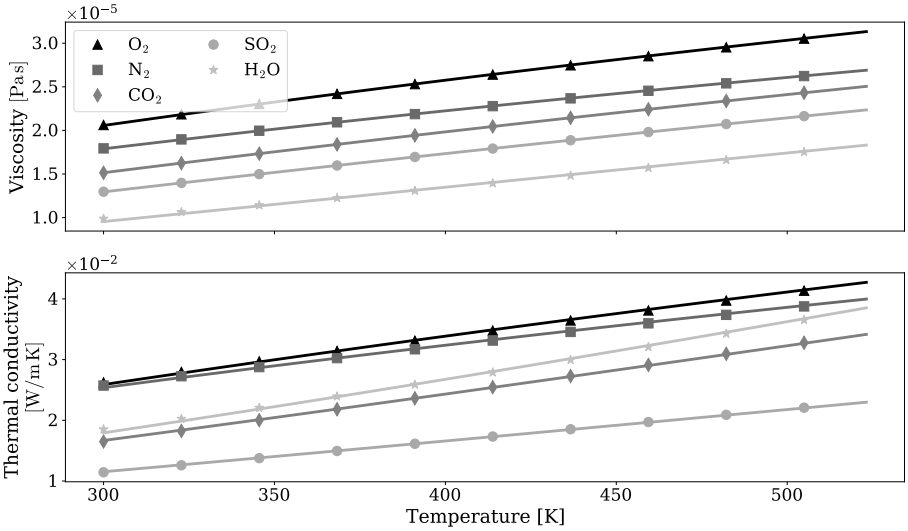

Fig. I.4: Viscosity and thermal conductivity for the species in the gas phase. The markers are derived from equation I.16 while the lines are derived from equation I.15, with the coefficients form table I.6

The coefficients found for the Sutherland equation are shown in table I.6 below:

specie	A_μ $\times 10^{-6}$	T_μ	A_κ $\times 10^{-3}$	T_κ
O_2	1.746	142.6	2.946	298.1
N_2	1.461	125.6	2.489	217.2
CO_2	1.656	268.0	5.148	1285.8
SO_2	1.662	366.8	2.968	1026.4
H_2O	2.281	960.7	16.22	4494.9

Table I.6: Viscosity and thermal conductivity coefficients for the Sutherland equation I.15. The coefficients are fitted to equation I.16 in the temperature range 300K-623.15K.

Although the lowest temperature of the range for which the coefficients are fitted does not cover the range experienced by the gas phase in the scrubber the range of extrapolation will not be more than 10K. Therefore it is assumed that this will not cause any significant errors.

I.4 Species diffusion

Diffusion coefficients

To estimate the diffusion coefficients of transferring species in the liquid phase Stoke-Einstein's equation is often used as a starting point for correlations [78]:

$$D_{AB} = \frac{kT}{6\pi r_A \mu_B} \tag{I.17}$$

Where A is the solute and B is the solvent. As the temperature of the liquid does not vary over a large range in the scrubber the relationship shown in Equation I.18 holds [79]:

$$\frac{D_{AB}\mu_B}{T} = const \tag{I.18}$$

Equating this to a know reference and assuming that the viscosity is independent of temperature. The diffusion coefficient for a species in a liquid can be given as:

$$D_{AB} = D^{\ominus}_{AB}\frac{T}{T^{\ominus}} \tag{I.19}$$

For species diffusing into the gas phase from the gas-liquid interface a simplified Chapman-Enskog equation is used as the parameters for the original expression is not readily available [56]. The expression for the gaseous diffusion coefficient is give as [80]:

$$D_{AB} = D^{\ominus}_{AB}\left(\frac{T}{T^{\ominus}}\right)^{3/2} \tag{I.20}$$

From equations I.19 and I.20 it can be seen that with the correlations used for the diffusion coefficients only a reference values for the coefficient and temperature are required. These are presented in Table I.7 below:

Specie	Solvent	$D^{\ominus}$ [kg/s]	$T^{\ominus}$ [K]	Ref.
SO_2	H_2O	1.54×10^{-8}	315.15	[81]
CO_2	H_2O	2.00×10^{-9}	298.15	[80]
SO_2	air	1.24×10^{-5}	293.15	[82]
CO_2	air	1.60×10^{-5}	298.15	[80]
H_2O	air	2.50×10^{-5}	298.15	[80]

Table I.7: Standard diffusion coefficients and temperature for the species transferring across the gas-liquid interface.

II Equilibrium constants

The equilibrium constant used for the chemistry model are presented in the following.

The equilibrium constants for the sulphite, bi-sulphite and sulphate equilibria, presented in equations 3.14, 3.15 and 3.16 can be given as [30, 83, 84]:

$$K_{HSO_3} = 1.727 \times 10^{-5} \exp\left(\frac{-1972}{T}\right) \tag{II.21}$$

$$K_{SO_3} = \exp\left(-358.57 + \frac{5477.1}{T} + 65.31\ \ln(T) - 0.1624T\right) \tag{II.22}$$

$$\begin{aligned} K^*_{SO_4} = \exp\Bigg(&-\frac{4276.1}{T} + 141.328 - 23.093\log(T) + \\ &\left(-\frac{13856}{T} + 324.57 - 47.986\log(T)\right)\sqrt{I} + \\ &\left(\frac{35474}{T} - 771.54 + 114.723\log(T)\right) I + \\ &\frac{-2698}{T} I^{1.5} + \frac{1776}{T} I^2\Bigg) \end{aligned} \tag{II.23}$$

The equilibrium constants for the carbon species presented in equations 3.5 and 3.4 have both been determined for seawater in the same work and are therefore expressed similarly as follows [31]:

$$\begin{aligned} \log(K) &= (A + A_0) + \frac{B + B_0}{T} + (C + C_0)\ln(T) \\ A &= a_0\sqrt{S} + a_1 S - a_2 S^2 \\ B &= a_3\sqrt{S} - a_4 \\ C &= a_5\sqrt{S} \end{aligned} \tag{II.24}$$

In tables II.8 and II.9 the coefficients for the bicarbonate and carbonate equilibria to be used with equation II.24 are presented:

$K^*_{HCO_3}$					
a_0	21.0894	a_3	-772.483	A_0	14.613358
a_1	0.1248	a_4	-20.051	B_0	5143.692
a_2	-3.68710^{-4}	a_5	-3.3336	C_0	-90.1833

Table II.8: Coefficients for the bicarbonate equilibrium.

$K^*_{CO_3}$					
a_0	13.4191	a_3	-530.1228	A_0	-126.34048
a_1	$0.0331S$	a_4	-6.103	B_0	6320.813
a_2	-5.33×10^{-5}	a_5	-2.0695	C_0	19.568224

Table II.9: Coefficients for the carbonate equilibrium.

Part II

Papers

Paper A

Heat and Mass Transfer Model for Droplets with Internal Circulation

Mathias Poulsen
Kim Sørensen
and
Thomas Condra

The paper has been published in the
Linköping Electronic Conference Proceedings Vol.176(25), pp. 175–202, 2021.

The layout has been revised.

Paper B

Comparison of Two-Phase Porosity Models for High Capacity Random Packing

Mathias Poulsen
Kim Sørensen
and
Thomas Condra

The paper has been published in the
E3S Web Conf. Vol. 321, 01015, 2021.

The layout has been revised.

Paper C

Optimisation of exhaust covers in marine scrubbers

Mathias Poulsen
Kim Sørensen
and
Thomas Condra

The paper is accepted for publication in the
Journal of Fluids Engineering

The layout has been revised.

Paper D

Development and calibration of a model for packed bed marine scrubbers aboard ocean-going vessels

Mathias Poulsen
Henrik Ström
Srdjan Sasic
Kim Sørensen
and Thomas Condra

The paper is under review

The layout has been revised.

ISSN (online): 2446-1636
ISBN (online): 978-87-7573-873-1

AALBORG UNIVERSITY PRESS